R. & M. No. 3483

R. & M. No. 3483

MINISTRY OF TECHNOLOGY

AERONAUTICAL RESEARCH COUNCIL
REPORTS AND MEMORANDA

Leakage and Secondary Flows in Compressor Cascades

By B. Lakshminarayana and J. H. Horlock

LONDON: HER MAJESTY'S STATIONERY OFFICE
1967
PRICE £1 5*s.* 6*d.* NET

Leakage and Secondary Flows in Compressor Cascades

By B. Lakshminarayana and J. H. Horlock

Department of Mechanical Engineering
The University of Liverpool

Reports and Memoranda No. 3483*
March, 1965

Summary.

This paper describes the effects of leakage and secondary flows on lift, outlet angles, induced drag and loss coefficients in a rectilinear cascade of compressor blades in which spanwise gaps simulated the clearance spaces of an axial compressor. The resultant leakage flow was studied under three different conditions, (i) with uniform inlet flow (ii) with non-uniform inlet flow near the gaps (iii) with severely non-uniform inlet flow and an end wall within the gaps.

In the first experiment only leakage flows were present. Analytical predictions of blade pressure distributions and induced drag agree fairly well with the experimental values. A semi-theoretical formula for induced drag coefficients is suggested for use by designers. For the range of gap/chord ratios used in practice, leakage produces a slight increase in the average lift.

In the second experiment an interaction between leakage and secondary flows was found to be generally favourable. The leakage and secondary flows are opposite in direction and this results in the angle distribution becoming more uniform and less variation in spanwise pressure distribution. Analytical predictions of outlet angle agree qualitatively with experimental values.

The leakage flow was found to have very favourable effects in the third experiment. The severe separation in the corner formed by the wall and blade suction surface that is observed when there is no clearance is reduced by the leakage flow. The outlet angle distribution becomes more uniform and the loss coefficients are reduced. An optimum gap/chord ratio, at which separation on the blade and wall surfaces is a minimum, is also observed.

CONTENTS

*Replace A.R.C. 26 821.

CONTENTS—*continued*

1. *Introduction.*

In recent years many efforts have been made to understand the flow in axial flow compressors. Inefficiency is due to skin friction on the blades and secondary losses. The boundary layers which build up on the annulus walls of the machine and the regions where the ends of the blades meet these walls are a major source of loss. A detailed classification of these secondary flows is given in Reference 1, and is summarized in Figure 1.

In a compressor cascade, with tip clearance between the blades and the end wall, deviations from two-dimensional flow are due to

(1) 'cascade' secondary flow: the annulus wall boundary layer, containing vorticity perpendicular to the streamwise direction, is deflected through the cascade of blades and a component of vorticity is produced in the streamwise direction

(2) leakage flow, caused by the unloading of the blade towards the tip.

The distributed vorticities produced in cascade secondary flow influence the pressures on the blade surfaces and the outlet-angle distribution. The secondary flow is substantially altered if leakage flow is allowed to take place at the blade tip. The vortices produced by secondary and leakage flows interact together to form a complicated vortex pattern.

An attempt is made in this paper to gain a better understanding of leakage flow and its effect on the lift distribution, induced drag, distributions of outlet angles, and the separations on the wall and blade surfaces. Attempts have also been made to understand the interaction of the leakage and cascade secondary flows and the resulting effects on outlet angles and losses.

The experiments described here form part of a series of experiments by Armstrong, Louis, Soderburg and a number of other authors:

(a) Studies of secondary flow (in the absence of tip clearance and a streamwise component of inlet vorticity) (Armstrong[24], Louis[20]),

(b) studies of secondary flow, in the absence of tip clearance but in the presence of a streamwise component of inlet vorticity (Soderberg[9], Horlock[25]),

(c) a study of leakage flow in the absence of both streamwise and normal components of inlet vorticity (the first experiments, A, described here),

(d) the effects of leakage flow when there is a normal component of vorticity at inlet (the second and third experiments, B and C, described here),

(e) secondary and leakage flow in the presence of both normal and streamwise components of inlet vorticity,

(f) secondary and leakage flow, in the presence of both normal and streamwise components of inlet vorticity, with relative motion between blades and wall.

In the first experiment (A) study of leakage flow in the absence of inlet vorticity was carried out in a cascade with centrally-split blades (Fig. 2a). In the absence of inlet vorticity there was no secondary flow so leakage flow only was present.

In the second experiment (B) a plate was inserted upstream of the cascade (Fig. 2b) to provide a nonuniform flow at inlet. Two types of flow were studied:

(i) with no central gap (zero gap/chord ratio); the simple weak secondary flow,

(ii) with a finite gap/chord ratio; leakage flow in the presence of a weak normal component of inlet vorticity. Distributions of lift, of outlet angles and stagnation pressures were measured. Flow on the blade surfaces was visualized in both cases.

In the third experiment (C) the tests of B(ii) were repeated with a thin rough wall in the centre of the gap, as shown in Fig. 2c. Here again two cases were investigated:

(i) with zero gap/chord ratio; the strong secondary flow,

(ii) with a finite gap/chord ratio; leakage flow in the presence of a strong normal vorticity component at the inlet.

The optimum clearance, at which the flow separation in the corner formed by the wall and blade suction surface was minimum, was also determined under these conditions.

2. *Analysis.*

2.1. *Leakage flow in the Absence of Entry Vorticity.*

2.1.1. *Induced drag.* Rains[13] and Vavra[2] have assumed that the leakage flow, resulting from the pressure difference across the tip, occurs in an annulus of height equal to the clearance height and that the leakage flow, perpendicular to the chord, rolls up into a vortex whose energy cannot be recovered. A criticism of such an analysis is that it does not take into account the effect of space/chord ratio. Further, perturbations in the flow at other spanwise positions are neglected.

A different type of analysis is given in this section. In a modified lifting line analysis (for the conditions of Experiment A) it is assumed that the lift is uniform along the blade span and that only a part of the bound vortex is shed off at the blade tip. This analysis seems to yield good results for the range of clearances used in turbomachinery practice. The actual flow phenomenon near the tip is very complicated, and a more realistic approach would be to assume that the vortices are shed all along the chord. Such an analysis would be similar to that proposed by Bollay[11] for small aspect-ratio wings.

Attempts[14] to predict the induced-drag coefficient using 'lifting-line theory', with the full bound vorticity shed along the blade trailing edge, were found to be unsatisfactory for the range of gap/chord ratios used in turbomachinery practice. Here a uniform spanwise circulation distribution is assumed together with a shed tip vortex of strength $(1-K)\Gamma_{2d}$ (where K is the fraction of lift retained at the tip). The perturbations to the flow along the lifting line caused by these tip vortices are calculated and the induced-drag coefficient derived therefrom.

The value of K will depend on various factors,

$$K = f(R_n, t/c, \lambda, s/c, \Gamma_{2d}) \tag{1}$$

Since theoretical prediction of K is extremely difficult, experimental values, extrapolated from lift distribution curves, have been used for numerical calculation of drag coefficients.

The vortex system assumed for this type of analysis is shown in Fig. 3.

Using Milne Thompson's analysis, Ref. 15, it can be proved that

$$v_{11} = \frac{(1-K)}{4s}\Gamma_{2d}\coth\frac{\pi z}{s} \tag{2}$$

$$v_{12} = \frac{-(1-K)}{4s}\Gamma_{2d}\coth\frac{\pi(z+2\tau)}{s} \tag{3}$$

where v_{11} is the induced velocity at any point z, due to one row of vortices

v_{12} is the induced velocity at z due to the other row of vortices.

Hence the total induced velocity at any point z is

$$v = v_{11}+v_{12} = \left[\frac{(1-K)}{4s}\Gamma_{2d}\right]\frac{\left[\coth^2\frac{\pi z}{s}-1\right]}{\left[\coth\frac{\pi z}{s}+\coth\frac{2\pi\tau}{s}\right]} \tag{4}$$

The induced drag is given by

$$D_{ic} = \int_{d/2}^{l} \rho v \Gamma dz \tag{5}$$

where d is the diameter of the tip vortex. The induced velocity at $z = 0$ becomes infinite so the vortices are taken to be of finite size.

Substituting equation (4) in (5) and knowing that

$$L = \rho U \Gamma$$

it can be proved that

$$C_{Dic} = \frac{C_L^2(1-K)}{8A} \int_{d/2s}^{l/s} \frac{\coth^2 \frac{\pi z}{s} - 1}{\coth \frac{\pi z}{s} + \coth \frac{2\pi\tau}{s}} d(z/s). \tag{6}$$

By expressing $\coth \frac{\pi z}{s}$ in terms of exponential functions it can be shown that,

$$C_{D_{ic}} = \frac{C_L^2(1-K)}{2A} \int_{d/2s}^{l/s} \frac{e^{2\pi z/s} d(z/s)}{\left(e^{2\pi z/s} - 1\right)\left[\left(e^{2\pi z/s} + 1\right) + \coth \frac{2\pi\tau}{s}\left(e^{2\pi z/s} - 1\right)\right]}. \tag{7}$$

This expression may be integrated, using a value of $d/2s = 0{\cdot}025$, obtained from the experimental results, to give

$$\frac{C_{D_{ic}}}{C_L^2(1-K)} = \frac{1}{8\pi A} ln \frac{\left(e^{2\pi l/s} - 1\right)\left(2{\cdot}17 + 0{\cdot}17 \coth \frac{2\pi\tau}{s}\right)}{0{\cdot}17\left[\left(1 - \coth \frac{2\pi\tau}{s}\right) + \left(1 + \coth \frac{2\pi\tau}{s}\right) e^{2\pi l/s}\right]}. \tag{8}$$

Using this expression calculations were made of the effect of space-chord ratio and passage aspect ratio (l/s) on the value of the induced-drag coefficient. The values obtained are plotted in Fig. 4.

A marked increase in drag coefficient at low-passage aspect ratio (l/s) is evident from Fig. 4.

The variation of losses with space/chord ratio (for the same blade loading) is very small. This is probably because interference effects due to tip vortices of adjoining blades and their images are opposite in direction and almost equal in magnitude.

2.1.2. *Blade pressure distribution.* The presence of a vortex close to the suction surface of the blade tip alters the blade pressure distributions in the tip region. Yakoyama[12] has made an attempt to predict such changes in pressure distribution by assuming the bound vortices leave the tip and join a vortex starting from the leading edge and inclined at an angle to the blade surface. The theory fails to explain spanwise irregularities in the lift distribution curve. By modifying Yakoyama's analysis a more realistic attempt is made at predicting the pressures on the blade surfaces. The analysis is for uniform inlet flow.

It is assumed that

(1) the strength of the vortices shed along the span is negligibly small, (i.e. only tip vortices are present),

(2) the strength of the bound vorticity varies linearly with x/c. [Because the circulation of a bound vortex is proportional to the pressure difference between the surfaces, the shape of the blade pressure distribution will be triangular (Fig. 5)],

(3) vortices leaving the tip join a vortex which starts from a point 0·25c from the leading edge. [Exploratory experiments[16] have revealed that these assumptions are valid for the range of gap/chord ratios (2 to 4 per cent) used in turbomachinery practice. It is implied from consideration of the bound vortex diagram that only 9/16 of the total bound vortex at the tip is shed off.]

(4) the shed vortex line is defined by the angles θ^* and $\bar{\omega}$ as shown in Fig. 5.

(5) The angles θ^* and $\bar{\omega}$ (Fig. 5) are small. No theoretical method of predicting their magnitude is given; experimentally observed values have to be used.

An expression for the induced velocity w at any point $D(x^*, y^*, z^*)$ is derived in Appendix A (Equations A6 and A14). The pressure distribution may then be determined from the relation (Reference 12)

$$C_p = C_{p2d} - \left(\frac{w}{U_1}\right)^2$$

2.2. *Secondary Flow in the Presence of a Normal component of Inlet Vorticity.*

Hawthorne[6], Loos[7], Smith[8], Soderberg[9] have considered the secondary motions induced by distributed secondary vorticity (ξ_s) in the flow between the blades. A streamfunction (ψ) for the secondary flow is defined and Poisson's equation $\nabla^2 \psi = -\xi_s$ is solved for ψ. Correlation between the solutions and experiments is good only when viscous effects are small and when there is no flow separation in the corner formed by the wall and blade suction surfaces. Louis[10] takes into account viscous effects in determining the secondary vorticity; his analysis has proved useful in predicting the outlet angles observed in Experiment B. The expressions for secondary and normal vorticity derived by Louis are given in Appendix B.

2.3. *Secondary and Leakage Flow in the Presence of a Normal Component of Inlet Vorticity.*

For the combined flow of Experiment B, the passage near the tip is filled with secondary and leakage vorticity.

A qualitative analysis has been carried by assuming the leakage vorticity is distributed throughout the passage (Appendix B). An expression derived for the total change in outlet angle,

$$\Delta\bar{\alpha}_2 = (\Delta\bar{\alpha}_2)_s + (\Delta\bar{\alpha}_2)_c \tag{9}$$

where the change in outlet angle due to secondary flow $(\Delta\bar{\alpha}_2)_s$ is obtained from Louis's theory (Appendix B.1) and the change in outlet angle due to leakage flow $(\Delta\bar{\alpha}_2)_c$ is given by the analysis in Appendix B.2.

3. *Experimental Results.*

3.1. *Experimental Equipment and Instrumentation.*

The low speed cascade tunnel No. 1 of the turbomachinery laboratory at Liverpool University was used for the experimental investigations.

A cascade with nine split blades of 10C430C50 Profile was set at 36 deg stagger (Plate 1). Other details of the cascade test were,

Aspect ratio of the unsplit blade	= 4·83
Space/chord ratio	= 1·00
Reynolds No. (with respect to a chord of 6 in.)	= 2×10^5
Air inlet angle	= 51 deg 53 min
Air outlet angle (two-dimensional)	= 31 deg

On one side of the cascade, the blades were cantilevered from a solid framework with an overhang of 9 in. On the other side of the cascade, five of the nine blades were mounted as a single movable unit sliding through the cascade walls (Plate 1). Accurate adjustment of the clearances between the tips was obtained and there was negligible bending or twisting of the cantilevered blades.

The centre blade had 35 hypodermic tubes embedded in it and holes were drilled in these tubes at distances of 1/100 in., 1/16 in., 1/8 in., 1/4 in., 1/2 in., 1 in., 2 in. and 6 in. from the blade tip, (the respective non-dimensional distances z/l are 0·00069, 0·0043, 0·0086, 0·0172, 0·0345, 0·069, 0·138 and 0·415), and these measuring stations are respectively referred to as A, B, C, D, E, F, G, and H. The pressure distributions were measured at any one of these positions by blanking off the other rows of tappings by means of adhesive tape 0·002 in. thick.

The non-uniform entry conditions required for Experiment B (Fig. 2b) were obtained by means of a perforated steel plate upstream of the cascade: the details are given in Reference 16. The trailing edge of this plate was 16 in. from the leading edge of the cascade. The total length of the plate in the streamwise direction was 18 in.

The steep inlet velocity gradient needed for Experiment C (Fig. 2c) was obtained by inserting a thin 'Masonite' wall with rough surfaces at the centre of the slot (Plate 2). The leading edge of this wall was flush with the trailing edge of the plate used in the previous experiment.

The inlet conditions for Experiment A were uniform and those for Experiments B and C are given in Figs. 7 and 8 respectively.

The experimental inlet velocity profile for Experiment B may be approximated by Schlichting's[17] empirical relation,

$$\frac{U_1}{U_{1\infty}} = 1-2B\left[1-\left(\frac{z}{\delta}\right)^{3/2}\right]^2$$

where B is constant for a particular wake (Fig. 7).

A vorticity meter mounted in miniature ball bearings[4] was used to assess the magnitude of shed vortex strength in Experiments A and B. All the vorticity measurements were made very near the trailing edge of the blade. The speed of the rotor was measured by means of a stroboflash.

A combined pitot and claw type yawmeter was used for outlet pressure and angle traverses. The measuring stations were at 1/2 chord upstream and downstream.

In three-dimensional flow, continuity is not necessarily satisfied along a pitch and hence a 'mass averaged' loss coefficient was computed from the following equations

$$\zeta = \frac{\int_0^s \rho U_2 \cos\alpha_2 (P_r - P_2)ds - \int_0^s \rho U_1 \cos\alpha_1 (P_r - P_1)ds}{\frac{1}{2}\rho U_r^2 \rho U_1 \cos\alpha_1 s}. \tag{10}$$

where subscript r refers to a reference condition upstream.
The first and second terms represent the stagnation pressure deficiency at outlet and inlet respectively. The second term is zero for uniform inlet flow.

The average loss coefficient defined for a specific region (of areas $s \times l$) is

$$\bar{\zeta} = \frac{1}{l}\int_0^l \zeta dl. \tag{11}$$

Qualitative pictures of the flow pattern on the blade surfaces were obtained with carbon black. The carbon black, which is available commercially, was suspended in paraffin oil and smeared over the blade surface. The tunnel was kept running for 1/2 to 1 hour until the last traces of the suspension dried up. The streamlines were then photographed.

The experiments carried out are summarized in Table 1.

TABLE 1

Experiment	Nature of the experiment	λ
Experiment A (Fig. 2a)	Uniform inlet flow	Varied
Experiment B (Fig. 2b)	Non-uniform inlet flow	0 and 0·04
Experiment C* (Fig. 2c)	End wall and steep inlet velocity gradient	0 and 0·04

*Flow visualization experiments were carried out for $\lambda = 0, 0{\cdot}02, 0{\cdot}04, 0{\cdot}06, 0{\cdot}08$.

The experimental data is presented in the following way. The blade pressure distributions for Experiment A are analysed to give the lift forces and the induced drag, and are compared with analytical predictions. The blade pressure distributions for Experiment B are analysed to give the lift forces (Section 3·2.). Stagnation pressure measurements and loss coefficients are compared for the three experiments (Section 3.3). Outlet angle distributions for the three experiments are compared in Section 3.4. Analytical estimates of outlet angle variation are given.

Results obtained using the vorticity meter and flow visualization give physical interpretations of the results of the three experiments and are described in Section 3.5 and 3.6 respectively.

3.2 *Blade Pressure Distributions*

3.2.1. *Experiment A (Leakage only).* Observed blade pressure distributions for $\lambda = 0{\cdot}01$, 0·04 and λ large are plotted in Fig. 9 (results with other gap/chord ratio are presented in Reference 16).

The presence of the leakage vortices near the suction surface decreases the pressures on both the blade surfaces. The curves of pressure distribution (Fig. 9) also suggest that the shed vortices are formed further forward along the chord for low gap/chord ratios.

For very small gap/chord ratios (Fig. 9) the change in lift beyond Station E ($z/l = 0{\cdot}0345$ from the tip) is negligibly small but for larger gap/chord ratios, the pressure distributions beyond Station E are also affected. In turbomachinery practice, the value of gap/chord ratio very rarely exceeds 0·06. For such conditions leakage flow will affect the blade pressure distribution for only about 5 to 8 per cent of blade length from the tip.

The pressure distribution diagrams were integrated to derive normal force coefficients (C_n) and these are plotted in Fig. 10. The decrease in suction pressure is sometimes greater than the decrease in pressure on the pressure surface. This accounts for a slight increase in normal force near the tip for low gap/chord ratios (Fig. 10). The strength of the tip vortices increases as the gap/chord ratio is increased, and there is an appreciable increase in suction pressures at moderate and large gap/chord ratios ($\lambda = 0{\cdot}04$ and 0·06). This is shown in both the pressure and normal-force distribution diagrams (Figs. 9 and 10).

It is evident from Fig. 10 that for gap/chord ratios of up to 0·06 only a part of the bound vortex at the tip is shed off; for higher gap/chord ratios bound vortices from other spanwise positions are also shed off. The normal-force coefficient has a maximum value a little inward from the tip (between 1 to 3 per cent of blade length) for all gap/chord ratios investigated. This is because the core of the leakage vortex is located inward from the tip and at an angle to the edge of the blade (*see* Section 3.5).

Another interesting feature is that the leakage flow appears to reduce the laminar and turbulent separation which is present on the blade suction surface near the tip in two-dimensional flow (Figure 9a).

A plot of the percentage decrease in normal-force coefficient averaged over the whole span, for different gap/chord ratios (Fig. 11), shows that for the range of clearances used in turbomachinery practice, there

is always a slight increase in average normal-force coefficient. In the particular case examined, the maximum normal force occurred for a gap/chord ratio of 6 per cent. Only for high gap/chord ratios is there a significant decrease in the normal-force coefficient.

The analysis given in Appendix A was used to predict the pressure distributions observed in Experiment A. The angles θ^* and $\bar{\omega}$ needed to calculate C_p (Fig. 5) were obtained experimentally by means of the vorticity meter. The value of $\bar{\omega}$, the angle between the axis of the leakage vortex and the edge of the blade, was calculated from the experimentally determined location of the vortex core. The values of the angles so obtained for $\lambda = 0{\cdot}03$ are

$$\theta^* = 12 \text{ deg}, \bar{\omega} = 5{\cdot}5 \text{ deg}.$$

The predicted values of C_p and the corresponding measured values are given in Fig. 12. Qualitative agreement between the theory and experiment was obtained; although agreement is reasonably good on the suction surface, there is considerable difference between the theoretical and experimental pressure-surface distributions.

The surprising increase in local normal-force coefficient a little away from the tip (Fig. 12e) is explained by the analysis, which assumes the vortices to be shed at an angle to the blade tip and blade suction surface.

The theory presented in Section 2.1.2 neglects the change in diameter of the vortex. In practice the vortex is in the form of a cone whose apex is somewhere along the chord (Fig. 13).

The drag coefficients were derived from the pressure distributions plotted on a line perpendicular to mean stream velocity of the cascade. A typical diagram at one spanwise position is given in Fig. 14. The area of such a diagram gives the form drag at zero gap/chord ratio and the (form plus induced) drag at a finite gap/chord ratio. The difference in area between these two provides the value of the induced drag. The average drag coefficient for the whole blade is then obtained from integration of the spanwise distribution of drag coefficient. Experimental values of drag coefficients so obtained are plotted in Fig. 15.

A knowledge of the fraction of lift retained at the tip is essential for the prediction of induced drag from the analysis presented in Section 2.1.1. These are obtained from extrapolation of the lift-distribution curves (Fig. 10). The values of retained lift are plotted in Fig. 16a.

With K, C_L and the other cascade parameters known, theoretical drag coefficients may be calculated from equation (8) (Fig. 15). Reasonably good agreement between theory and experiment justifies the method of calculation given in Section 2.1.1.

The variation with l/s of the quantity $\dfrac{C_{D_{ic}}A}{(1-K)C_L{}^2}$ in equation (8) is small for moderate values of τ/s (Fig. 16). The $\left(\dfrac{C_{D_{ic}}A}{(1-K)C_L{}^2}\right) - \tau/s$ relation can be approximated by a straight line as shown in Fig. 16b, from which the following relationship is derived

$$C_{D_{ic}} = 1{\cdot}4\frac{(1-K)C_L^2}{\mathrm{A}}\left(\frac{\tau}{s}\right). \tag{12}$$

For the range of clearances used in turbomachinery practice, the values of K can be assumed to be 0·5 (Fig. 16a). Hence equation (13) can be reduced to

$$C_{D_{ic}} = 0{\cdot}7\frac{C_L^2}{A}\left(\frac{\tau}{s}\right). \tag{13}$$

Agreement between this equation and experiment (Fig. 15) is reasonably good and it is suggested for use by designers. It may be noted that a similar empirical correlation has been suggested by Ainley[18,19] for evaluating losses due to leakage flow in a turbine,

$$C_{D_{ic}} = 0{\cdot}5\frac{C_L^2}{A}\left(\frac{\tau}{s}\right).$$

Fujie,[3] basing his argument on Vavra's[2] analysis, has suggested an empirical drag coefficient due to clearance. His expression is

$$C_{D_{tc}} = 0{\cdot}29(\tau/l)C_L^{3/2}\,. \tag{14}$$

This expression is compared with the author's theoretical and experimental values in Fig. 15. Fujie's relationship seems to provide optimistic values.

3.2.2. *Experiment B* (*Weak secondary flow and leakage*). The blade pressure distributions (based on inlet local dynamic head) obtained from Experiment A ($\lambda = 0{\cdot}04$) and Experiment B ($\lambda = 0$ and $0{\cdot}04$) at distances $0{\cdot}00069l$ and $0{\cdot}0172l$ from the blade tip are compared in Fig. 17. For zero gap/chord ratio in Experiment B, the pressure coefficients near the trailing edge of the suction surface of the blade tip are lower than the two-dimensional values. This is probably due to separation on the blade suction surface near the trailing edge. For $\lambda = 0{\cdot}04$ there is an improvement in the pressure distributions on both pressure and suction surfaces in Experiment B. This appears to be due to the opposing effects of secondary flow and leakage, and to viscous effects inside the gap.

A study of the peak pressures on the suction side of the blade for various cases examined (Fig. 17) indicates that the leakage vortices are formed further forward along the chord in the case of non-uniform inlet flow.

The spanwise distributions of normal-force coefficient (based on inlet local dynamic head) are plotted in Fig. 18. An appreciable increase in normal-force coefficient near the blade tip observed in Experiment B ($\lambda = 0{\cdot}04$) is associated with overturning of the fluid and the presence of the leakage vortices near the suction surface. Underturning due to the secondary flow tends to decrease the normal-force coefficient beyond $z^1 = \delta/2$.

3.3. *Stagnation Pressure Distributions at Outlet.*

Traverses of stagnation pressure at outlet covered an area 8 in. across the passage and 5 in. along the span.

3.3.1. *Experiment A* (*Leakage flow only*). The presence of a strong vortex core is evident from Fig. 19a. The leakage flow has very little effect beyond $z'/l = 0{\cdot}11$. The tendency of the leakage flow to roll up and form discrete vortices is also evident from the total-pressure contours.

3.3.2. *Experiment B* (*Weak secondary flow and leakage*). Contours of dynamic head for $\lambda = 0$ and $0{\cdot}04$ are plotted in Fig. 19b and c respectively.

The secondary flow is directed towards the centre of the wake on the pressure side and away from it on the suction side. Heavy losses near the wake centre below the suction surface are caused by flow separation.

The dominant effect of leakage flow can be clearly seen in Fig. 19c up to 1/6th of blade span from the wake centreline (for $\lambda = 0{\cdot}04$). Induced flow towards the tip of the blade suction surface eliminates the separation zone observed for $\lambda = 0$ (Fig. 19b).

The secondary and leakage flows are in opposite directions (Fig. 20) and they meet to form a core of heavy losses in the mid-passage at exit. In the particular case examined, the effect of secondary flow is overshadowed by leakage flow. The leakage flow helps to keep the separation on the blade suction surfaces at a minimum.

On the other hand, the favourable effect of secondary flow on leakage losses is clear from a comparison of Experiments A and B (Figs. 19a and c). The secondary flow reduces the losses in the shed vortex core, but spreads the losses over a wider area.

Loss coefficients derived from equation (10) for $\lambda = 0$ and $0{\cdot}04$ (Experiments A and B) are plotted in Fig. 21a.

The negative values of loss coefficients obtained for non-uniform inlet flow are due to spreading of the wake as it passes through the cascade. The stagnation pressure deficiency near the wake centre at the inlet is greater than at outlet.

The loss coefficients averaged over the whole span ($\bar{\zeta}$) and the percentage increase over the two-dimensional values (with uniform upstream flow and $\lambda = 0$) are given in Table 2.

TABLE 2

Average Loss Coefficients for Experiments A and B

Experiment	λ	Inlet Flow	$\bar{\zeta}$	$\left(\frac{\bar{\zeta}_{3d}-\bar{\zeta}_{2d}}{\bar{\zeta}_{2d}}\right)\times 100$
A	0	Uniform	0·024	0
A	0·04	Uniform	0·032	31
B	0	Non-uniform	0·028	16
B	0·04	Non-uniform	0·034	41·6

Losses due to leakage are clearly significant.

3.3.3. *Experiment C (Strong secondary flow and leakage).* Contours of dynamic head are given in Fig 22a (for $\lambda = 0$) and Fig. 22b (for $\lambda = 0{\cdot}04$).

The strong secondary flow near the wall causes the boundary layer to accumulate in the corner formed by the wall and blade suction surface. Large areas of separation are evident for $\lambda = 0$, Fig. 22a, spreading as far as $0{\cdot}24l$ from the wall. The losses due to separation should be distinguished from the losses due to secondary flow alone. In conducting similar experiments Louis[20] observed such separation even with uniform upstream flow. The secondary flow in his experiments was weak but the losses due to separation of the flow, in the corner formed by the blade suction surface and wall, were high as in the present case.

The loss core is located a little away from the suction surface and near the wall for $\lambda = 0$ (Fig. 22a); it moves nearer to the suction surface but away from the wall for $\lambda = 0{\cdot}04$ (Fig. 22b). This movement is caused by the leakage flow which tends to 'wash away' the separation zone observed for $\lambda = 0$. The opposing secondary flow pushes the leakage vortices near to the suction surface but away from the tip.

The loss coefficients for Experiments C ($\lambda = 0, \lambda = 0{\cdot}04$), are plotted in Fig. 21 b. The effect of leakage is to decrease the loss coefficients at most spanwise positions.

The loss coefficients averaged over the span are given in Table 3.

TABLE 3

Average Loss Coefficients for Experiment C

Experiment	λ	Inlet Flow	$\bar{\zeta}$	$\left(\frac{\bar{\zeta}_{3d}-\bar{\zeta}_{2d}}{\zeta_{2d}}\right)\times 100$
A	0	Uniform	0·024	0
C	0	Steep inlet velocity profile	0·037	54
C	0·04	Steep inlet velocity profile	0·027	12·5

Comparison of the losses observed in Experiments B and C (Tables 2 and 3) shows that the combined losses due to separation and secondary flow (for $\lambda = 0$) are increased three fold in Experiment C, whereas the total losses for $\lambda = 0{\cdot}04$ are reduced drastically.

3.4. *Angle Distribution at Outlet.*

3.4.1. *Experiment A (Leakage flow only).* Contours of outlet angle for $\lambda = 0{\cdot}04$ (Fig. 23a) show large underturning near the tip, especially at mid-passage, caused by the leakage vortex. The leakage flow affects the outlet angle up to $z/l = 0{\cdot}16$. A plot of average outlet angle shows large underturning up to $z/l = 0{\cdot}06$ and slight overturning beyond this location (Fig. 25).

3.4.2. *Experiment B (Weak secondary flow and leakage).* Contours of outlet angle for $\lambda = 0$ and $0{\cdot}04$ are given in Fig. 23b and c. For $\lambda = 0$, overturning near the wake centre at mid-passage is caused by secondary flow.

For $\lambda = 0{\cdot}04$, there is a substantial change in outlet angle near the suction surface due to leakage flow which overshadows disturbances caused by secondary flow.

From Fig. 20, in which the nature of leakage and secondary flows in a cascade are shown qualitatively, it can be seen that the leakage flow opposes the secondary flow in most of the channel between the blades. Thus when leakage flow is allowed to take place the region of overturning observed for $\lambda = 0$ (Fig. 23b) is completely eliminated. Furthermore the underturning observed for $\lambda = 0$ is replaced by overturning near the blade suction surface. The leakage flow influences almost the whole flow field inside the wake even though its effect is most pronounced near the suction surface at the blade tip.

It can also be seen from Figs. 23a and c that the effect of secondary flow is to move the leakage vortices nearer to the blade suction surface. The maximum underturning observed for $\lambda = 0{\cdot}04$ (Fig. 23c) is 24 deg and the maximum overturning is 4 deg. The corresponding figures for the same gap but with uniform inlet flow (Experiment A) are 30 deg and 9 deg respectively. The effect of secondary flow on leakage is to some extent favourable, as is also indicated by the normal-force distributions plotted in Fig. 18.

The average outlet angles obtained from all these experiments (A and B) are plotted in Fig. 25. It is clear from this plot that the combined leakage and secondary flows produce smaller changes in average outlet angle.

Predicted angle distributions from Louis's[10] analysis (for simple secondary flow, $\lambda = 0$) and the author's analysis (for combined secondary and leakage flows) are plotted in Fig. 26.—Appendix B.

There is reasonably good agreement between Louis's[10] theory and authors' experiment. A further discussion of predictions of outlet angle due to the secondary flow is given in References 21 and 22.

For $\lambda = 0{\cdot}04$, the angles were predicted from the analysis presented in Appendix B2. The experimental values of K used for this analysis are taken from Fig. 16a. Knowing $(\Delta\alpha_2)_s$ from Louis's[10] theory and $(\Delta\alpha_2)_e$ and from the authors' theory (Appendix B2), the total change in outlet angle can be calculated. The values so obtained are plotted in Fig. 26. The agreement between the theory and experiment (for $\lambda = 0{\cdot}04$—Fig. 26) is reasonably good near the blade tip but increasing discrepancies can be seen near $Z = \delta$. The sinusoidal distribution of leakage vorticity assumed for the analysis is of doubtful validity near the edge of the wake.

3.4.3. *Experiment C (Strong secondary flow and leakage).* Contours of outlet angle for Experiment C, for $\lambda = 0$, are plotted in Fig. 24a. At mid-passage, the usual secondary-flow effects are seen; overturning near the wall and underturning away from it, but the overturning takes place only in a small region. The underturning in the rest of the region is caused by flow separation in the corner formed by the wall and blade suction surface. Fig. 27 shows the outlet angles averaged over the passage (for $\lambda = 0$); there is large underturning for a considerable distance along the span.

For a finite gap ($\lambda = 0{\cdot}04$—Fig. 24b) the leakage flow tends to 'wash' away the separation zone on the blade and wall surfaces. The other interesting feature (Fig. 24b) is that, unlike the previous experiment in which the leakage flow dominated, the secondary flow now strongly opposes the leakage flow and prevents it moving further down the suction surface along the blade passage.

The interaction between the leakage and secondary flow is complicated. The effects of leakage are confined to a region near the suction surface, and the flow elsewhere is greatly influenced by secondary flow and separation. The effect of leakage, in the particular case examined, is to increase the underturning

below the suction surface near the wall and decrease the underturning (caused by separation) in most other regions (Fig. 27). To this extent the leakage flow greatly improves the lift distribution along the blade.

3.5. *Vorticity Measurements.*

Vorticity measurements were made in the outlet flow in Experiments A and B, using the small rotor described in Section 3.

3.5.1. *Experiment A (Leakage flow only).* Fig. 28a, in which the numbers denote the r.p.m. of the rotor, shows the comparative strength and location of the leakage vortices at various gap/chord ratios. For very low gap/chord ratios the leakage flow first appears as a vortex sheet parallel to the blade tip, which then rolls up into a discrete vortex away from the blade suction surface. At higher gap/chord ratios the leakage flow tends to roll up into a discrete vortex as soon as it reaches the suction surface of the blade. As λ is increased the core of the leakage vortex tends to move nearer to the suction surface, but further away from the tip. No trailing vortices were observed at other spanwise positions even for $\lambda = 0{\cdot}06$.

3.5.2. *Experiment B (Weak secondary flow and leakage).* The vorticity meter was not sensitive enough to make a qualitative study of the secondary vortices for $\lambda = 0$. The isospeed contours are given only for $\lambda = 0{\cdot}01$, $0{\cdot}04$ and $0{\cdot}06$ (Fig. 28b).

A comparison of Figs. 28 a and b shows the considerable effect of the secondary flow on the leakage flow. Because of the opposing secondary flow (Fig. 20), the leakage vortices tend to roll up nearer the suction surface (Fig. 28b).

The reduced r.p.m. of the rotor shows the effect of secondary flow in reducing the strength of leakage vortices. For very low gap/chord ratios, the magnitude of leakage flow is small and the shed vortices are of very low strength as shown in Fig. 28b ($\lambda = 0{\cdot}01$). For higher gap/chord ratio, the leakage flow is stronger, but the secondary flow spreads the leakage fluid along the span.

3.6. *Flow Visualization.*

Flow visualization experiments were carried out using the lamp black technique described in Section 3. Only the suction surface of the blade was photographed.

3.6.1. *Experiment A (Leakage flow only).* Plate 3 shows the streamline traces in carbon black for $\lambda = 0{\cdot}04$. It is evident from these streamline traces that leakage reduces or eliminates laminar and turbulent separations near the blade tip which are present in two-dimensional flow.

The flow phenomena near the tip of the blade are very complicated. The fluid particles are sucked in towards the core of the leakage vortex. This sets up a small spanwise flow, towards the tip, near the leading edge of the blade. Spanwise flow towards the tip was also observed on the pressure surface but is not shown in the photograph of the blade.

The flow pattern near the trailing edge of the blade tip (suction surface) shows a separation immediately downstream of mid-chord but this flow tends to re-attach near the trailing edge. This phenomena will be referred to as 'leakage separation'.

3.6.2. *Experiment B (Weak secondary flow and leakage).* The streamline traces for non-uniform inlet near the tip are shown in plate 4, for $\lambda = 0$ and $0{\cdot}04$.

For $\lambda = 0$ (plate 4a) the traces at midspan indicate a spanwise flow away from the wake centre. A spanwise flow towards the wake centre was also observed on the pressure surface but is not shown in the photograph.

The presence of a strong leakage vortex and the consequent induced flow is evident from Plate 4b. Comparing this with Plate 3, it can be seen that the spanwise flow is lessened. The reduction in 'leakage separation' on the blade suction surface of the tip is also evident.

3.6.3. *Experiment C (Strong secondary flow and leakage).* The flow on the wall and blade surfaces was visualized at various gap/chord ratios. An optimum clearance, at which the separation zones on the wall and blade surface are least, was determined.

For $\lambda = 0$ (Plate 5a) the separations on the wall and blade suction surface are very severe. For $\lambda = 0{\cdot}02$ (Plate 5b) leakage flow partly reduces the separation on the blade and wall surfaces near the tip. But the flow region is greatly influenced by flow separation and secondary flow, as is evident from the spanwise flow that occurs on the blade suction surface. When the gap/chord ratio is increased further (Plate 5c), the enhanced leakage flow tends to diminish the effects of secondary flow and separation considerably.

For large gap/chord ratios (Plates 5d and e) the excessive leakage increases the leakage separation on the blade suction surface. This is confirmed by the presence of a strong spanwise flow towards the tip on the blade suction surface.

There is an optimum clearance ($\lambda = 0{\cdot}04$ in the particular case examined) at which the separations on the blade and wall surfaces are a minimum.

The flow on the blade and wall surfaces (as revealed in Plates 5a to e) can be represented diagrammatically as shown in Fig. 29. For $\lambda = 0{\cdot}02$, the leakage and induced flows are not strong and are unable to 'wash away' the separations on wall and blade surfaces completely. For $\lambda = 0{\cdot}04$, the leakage flow moves much further along the suction surface and sweeps some of the boundary layer off the wall before rolling up in to a leakage vortex. The loss core moves farther away from the wall, and the strong leakage vortices induced greater spanwise flow which is responsible for a considerable reduction in separation on the blade suction surface. For $\lambda = 0{\cdot}06$, the leakage flow is very large and tends to roll up as soon as it reaches the suction surface (*See* also Ref. 4). This is evident from the increased separation on the wall and blade suction surface that is observed when λ is increased from 0·04 to 0·06.

4. *Discussion and Conclusions.*

4.1. *Experiment A (Leakage flow only).*

The approximate theory presented for the calculation of pressure distribution on the blade surfaces predicts qualitatively the increase in suction pressures and the peak values of normal-force coefficients that are observed a little inward from the tip.

For low and moderate gap/chord ratios there is a slight increase in the average lift. Only for very high gap/chord ratio is there a substantial decrease in lift.The leakage flow affects pressure distributions for about 5 to 8 per cent of the blade length from the tip for the range of gap/chord ratios used in practice. A part of this length experiences an increase in the normal force. Leakage flow causes large underturning near the tip and a slight overturning a little away from it. Flow visualization experiments suggest that the fluid is sucked in towards the vortex core and this gives rise to spanwise flow towards the tip of the suction side of the blade.

The expression for drag coefficient suggested by the authors in Equation (13) should be used with caution as the relative motion between the wall and the blade which may increase the leakage flow and hence the losses in compressor blades. The presence of a normal component of inlet vorticity, giving rise to secondary flow inside the passage, may reduce the leakage flow and hence the losses (as in Experiment B).

The analysis suggests that the losses are higher for blades of low-passage aspect ratio.

4.2. *Experiment B (Leakage flow with weak secondary flow)*

Experiment B shows that the effect of secondary and leakage flows on each other is to reduce the disturbance in the outlet flow.

For a finite gap/chord ratio there is a slight increase in the normal-force coefficient (based on inlet local dynamic head) near the tip, compared with that for uniform inlet flow atthe same gap/chord ratio. This is partly due to overturning of the flow caused by the secondary flow and partly due to the presence of leakage vortices near the suction surface of the blade. A little inward from the blade tip (near the edge of the wake) there is a slight decrease in the normal-force coefficient, due to underturning caused by the secondary flow.

The effect of leakage flow on the outlet angle distribution is opposite to that caused by secondary flow alone. Leakage flow causes underturning near the tip and small overturning away from it. The change in outlet angle due to leakage flow can be predicted qualitatively, if the retained lift at the tip is known.

Spanwise flows on the blade surfaces near the tip caused by secondary and leakage flows are in opposite directions on the suction surface. Vorticity measurements indicate that the secondary flow prevents the leakage flow from moving far along the end wall. The leakage flow tends to roll up to form a leakage vortex that is located nearer the suction surface than that observed with uniform inlet flow.

4.3. *Experiment C (Leakage flow with strong secondary flow).*

Experiment C shows that the leakage flow reduces the separation on the blade and wall surfaces. It appears that flow separation and velocity profile deterioration are not due to clearance effects.

The secondary flow causes the boundary layer to move parallel to the wall towards the suction surface. The opposite leakage flow prevents this flow from accumulating in the corner formed by the wall and blade suction surface. The net mixing effects are complicated and depend on the magnitude of the individual components. If the secondary flow is stronger than leakage flow, the low energy fluid will still accumulate in the corner, but to a lesser degree than it does with no leakage. If the leakage flow is stronger, the accumulation is prevented but a stronger leakage vortex forms near the suction surface.

Presence of a leakage vortex induces spanwise flow towards the tip on the suction surface and hence helps to keep the separation zone on this surface at a minimum. If the leakage flow is strong, a 'leakage separation' forms on the blade suction surface near the tip.

At some intermediate gap/chord ratio, the leakage flow is just strong enough to 'wash away' the separation zone on the wall and blade surfaces and the opposing spanwise flows on the blade suction surface (induced by leakage and secondary vortices) are nearly equal. For the particular cascade configuration tested this optimum gap/chord ratio was found to be 4 per cent.

The presence of such an optimum tip clearance has also been confirmed by Dean [23] and Hubert[5]. This is evident from Fig. 30a, where the loss coefficients for various gap/chord ratios obtained from Hubert and Dean are plotted. The presence of an optimum tip clearance, at which average normal-force coefficients are maximum, is evident from Fig. 30b reproduced from Dean's[23] report. The surprising conclusion is that very small clearances, difficult to incorporate because of mechanical limitations, are not always desirable.

Acknowledgement.

The authors wish to thank Mr. H. Ainsworth and his staff for their help in the construction of the experimental equipment.

LIST OF SYMBOLS

The notation used is illustrated in Figs. 2, 3, 4, 5 and 14.

$A = l/c$ = Aspect ratio of the blade

$A_p = l/s$ = Passage aspect ratio of the cascade

a = Speed of sound

c = Chord length of the blade

$K = C_{L_R}/C_{L_{2d}}$ = Fraction of lift retained at the tip

$2l$ = Total length of the unsplit blade

R_n = Reynolds number

s = Blade pitch

s' = $s \cos\alpha_2$

t = Blade thickness

T = Distance defined in Fig. 14

U = Fluid velocity

v = Velocity induced normal to lifting line of the blade

w = Small perturbation in the spanwise velocity

L = Lift force perpendicular to vector mean velocity (per unit blade span)

D_i = Induced drag force parallel to vector mean velocity.

N = Normal force perpendicular to blade chord

C_L = Lift coefficient based on inlet dynamic head

C_n = Normal force coefficient based on inlet dynamic head

$C_p = \dfrac{p-p_1}{\frac{1}{2}\rho U_1^2}$ = Blade pressure coefficient based on inlet dynamic head

$C_{D_i} = \dfrac{D_i}{\frac{1}{2}\rho U_1^2 cl}$ = Induced drag coefficients based on inlet dynamic head

P = Stagnation pressure

p = Static pressure

q = Scalar of velocity at any point along streamline, non-dimensionalized with respect to inlet velocity.

x, y, z = Co-ordinate system with origin at the leading-edge of the blade tip as shown in Fig. 2a.

x', y', z' = Co-ordinate system with origin at the centre line of the gap as shown in Figs. 2a and b.

x^*, y^*, z^* = Co-ordinate system used in the prediction of blade pressure distribution (Fig. 5).

X, Y, Z = Co-ordinates used at outlet of the cascade (Figs. 2b and c).

α = Air angles measured from axial direction of the cascade.

$\bar{\alpha}_2$ = Outlet angle averaged over pitch.

Γ = Total circulation around the profile.

γ = Circulation of the bound vortex.

Δ = A small change in value.

δ = Boundary-layer thickness or half the width of the wake.

$\varepsilon = \alpha_1 - \alpha_2$ = Turning angle of the cascade.

ζ = Loss coefficient.

$\bar{\zeta}$ = Loss coefficient averaged over the whole blade length.

θ^* = Angle between blade suction surface and axis of the leakage vortex (Fig. 5).

$\bar{\omega}$ = Angle between the blade edge and the axis of the vortex (Fig. 5).

$\lambda = \tau/c$ = Gap/chord ratio.

ν = Kinematic viscosity.

ξ = Streamwise component of vorticity.

Ω = Component of vorticity normal to streamlines.

ρ = Density of the fluid.

$\sigma = s/c$ = Space/chord ratio.

2τ = Gap width of a split blade or twice the tip clearance height in the case of a compressor.

ψ = Stream function.

ϕ = Potential function

η = Chordwise co-ordinate used to express the circulation distribution (*See* Fig. 5).

$\nabla^2 = \dfrac{\partial^2}{\partial y^2} + \dfrac{\partial^2}{\partial z^2}$

Subscripts

1 = Inlet.

2 = Outlet.

c = Due to leakage flow.

$2d$ = Two-dimensional

$3d$ = Three-dimensional

m = Mean.

r = Reference value at inlet.

R = Retained at the tip.

s	=	Due to secondary flow.
loc	=	Local.
max	=	Maximum.
shed	=	Shed vortex.
∞	=	Values outside non-uniform region.

Superscripts

$''$	=	Values with reference to inlet local dynamic head.
$-$	=	Average values.

REFERENCES

No.	Author(s)	Title, etc.
1	B. Lakshminarayana and J. H. Horlock	Secondary flows and losses in cascades and axial flow turbomachines. *Int. J. Mech. Sci.*, Vol. 5, pp. 287–307, 1963.
2	M. H. Vavra	*Aerothermodynamics and flow in turbomachines.* p. 381. John Wiley & Sons, New York, 1960.
3	K. Fujie	A study of the flow through the rotor of an axial compressor – Formulation of drag coefficients. *Bull. Japan. Soc. Mech. Engrs.*, Vol. 5, No. 18, 1962.
4	B. Lakshminarayana and J. H. Horlock	Tip-clearance flow and losses for an isolated compressor blade. A.R.C. R. & M. 3316, June 1962.
5	G. Hubert	Untersuchungen uber die sekundarverluste in axialen turbomachinen. *VDI Forschungsheft* 496, *VDI Verlag, GMBH Dusseldorf*, 1963.
6	W. R. Hawthorne	Some formulae for the calculation of secondary flow in cascades. A.R.C. Report 17519. March 1955.
7	H. G. Loos	Analysis of secondary flow in the stator of an axial turbomachine. Tech. Report No. 3, Jet Propulsion Lab., California Institute of Technology (USA) 1953.
8	L. H. Smith Jr.	Secondary flow in axial turbomachinery. Trans. Am. Soc. Mech. Engrs. Vol. 77, pp. 1065–1076, 1955.
9	C. R. Soderberg	Secondary flow and losses in a compressor cascade. Report 46, M.I.T. Gas Turbine Lab. (USA) 1958.
10	J. F. Louis	Rotational viscous flow. *Proceedings of the 9th Int. Cong. App. Mechs. (Brussels)*, Vol. III, p. 306–317, 1956.
11	W. A. Bollay	A non-linear wing theory and its application to rectangular wings of small aspect ratio. *Z. angew. Math. Mech.* Bd.19, No. 1, 1939. pp. 21–35.
12	A. Yakoyama	Comparative study of tip clearance in compressors and turbines. Gas Turbine Laboratory, M.I.T. (USA) Report No. 63, 1961.
13	D. A. Rains	Tip clearance flow in axial flow compressors and pumps. *Cal. Inst. Tech.* (USA) Mech. Eng. Lab. Report. 5, 1954.
14	B. Lakshminarayana	Extension of lifting line theory to a cascade of split aerofoils. *Am.Inst.Aero.Astro. Journal.* Vol. 2. May 1964. p. 938–940.
15	L. Milne-Thomson	*Theoretical hydrodynamics.* Macmillan Co. (Lond.) p. 374, 1960.

REFERENCES—*continued*

No.	*Author(s)*	*Title, etc.*
16	B. Lakshminarayana	Leakage and secondary flows in axial compressor cascades. Ph.D. Thesis, Liverpool University, 1963.
17	H. Schlichting	*Boundary layer theory.* McGraw-Hill Book Co., New York. p. 601, 1960.
18	D. G. Ainley and .. .. G. C. R. Mathieson	A method of performance estimation for axial flow turbines. A.R.C. R. & M. 2974, 1951.
19	D. G. Ainley and .. .. G. C. R. Mathieson	Examination of the flow and pressure losses in blade rows of axial flow turbomachines, A.R.C. R. & M. 2891. March 1951.
20	J. F. Louis	Secondary flow in compressor cascades. A.R.C. R. & M. 3136. March 1958.
21	J. H. Horlock, J. F. Louis, P. M. E. Percival and B. Lakshminarayana ..	Wall stall in compressor cascades. *J. bas. Engng.* Vol. 88D No. 3, p. 637 (1966).
22	B. Lakshminarayana and J. H. Horlock ..	Effect of shear flows on the outlet angle in axial compressor cascades. Methods of prediction and correlation with experiments. *J.bas.Engng. Vol.* 89 *D No.* 1 *p.* 191 (1966).
23	R. C. Dean	Influence of tip clearance on boundary layer characteristics in a rectilinear cascade. Rep. No. 27–3, Gas Turbine Lab., M.I.T. (USA) 1954.
24	W. D. Armstrong	The non-uniform flow of air through cascade of blades. Ph.D. Thesis, Cambridge University (1954).
25	J. H. Horlock	Annulus wall boundary layers in axial compressor stages. *J. Basic Eng.*, Vol. 85D. p. 55. (1963).

APPENDIX A

Prediction of Blade Pressure Distribution.

A.1. *Spanwise Induced Velocity.*

Fig. 5 shows the geometrical location of the leakage vortices and the notation used in the analysis.

According to Biot-Savart's Law the velocity induced at $D(x_1^*, y_1^*, z_1^*)$ by a segment $(ds)_1$ of one of the tip vortices,

$$\frac{1}{2\pi}\int_0^\infty \frac{\Gamma_0(\eta)\sin\theta_1 . ds}{r_1^2} \tag{A1}$$

Similarly the velocity at D due to a segment $(ds)_2$ of the other tip vortex is

$$-\frac{1}{2\pi}\int_0^\infty \frac{\Gamma_0(\eta)\sin\theta_2\, ds}{r_2^2}$$

where s = distance from leading edge along the tip vortex line, and $\Gamma_0(\eta)$ = total circulation at any point along the vortex line.

Knowing that

$$ds = d\eta/\cos\theta^* . \cos\bar{\omega} \tag{A2}$$

$$\Gamma_0(\eta) = \frac{2\Gamma_{2d}}{c^2}\left(\frac{3}{4}c\eta - \frac{\eta^2}{2}\right) \text{ for } 0 < \eta < \frac{3}{4}c \tag{A3}$$

and

$$\Gamma_0(\eta) = \frac{9}{16}\Gamma_{2d} \qquad \text{for } \eta > \frac{3}{4}c \tag{A4}$$

where

$$\Gamma_{2d} = U_1 \cos\alpha_1\, s(\tan\alpha_1 - \tan\alpha_2) \tag{A5}$$

it can be proved (Ref. 16 pp. 192–197) that the spanwise component of induced velocity (w) at D is given by

$$\frac{w}{U_1} = \frac{6\cos\alpha_1 . s(\tan\alpha_1 - \tan\alpha_2)}{16\pi c . \cos\bar{\omega}\sec^2\theta^*}\left\{F_1 R_1'\left[\frac{-8}{6c}\ln\frac{-x_1^*\cos\theta^* + \sqrt{R_1^2 + x_1^{*2}\cos^2\theta^*}}{\mathscr{R} + \sqrt{R_1^2 + \mathscr{R}^2}} - \right.\right.$$

$$-\frac{8}{cR_1^2}\left[\left(\frac{3}{4}c\sec\theta^* - \frac{x_1^*}{2}\cos\theta^*\right)\sqrt{R_1^2 + x_1^{*2}\sin^2\theta^*} + \cos\theta^* \times\right.$$

$$\left.\times\frac{\left(-\frac{9}{8}x_1^* c^2\sec^2\theta^* + \frac{3}{4}R_1^2 c.\sec^2\theta^* + \frac{9}{4}x_1^{*2}c - x_1^* R_1^2 - x_1^{*3}\cos^2\theta^*\right)}{2\sqrt{R_1^2 + \mathscr{R}^2}}\right] +$$

$$\left.\left. + \frac{3}{4}\frac{c\sec^2\theta^*}{R_1^2}\left(\frac{\mathscr{R}}{\sqrt{R_1^2 + \mathscr{R}^2}} - \cos\theta^*\right)\right] \right. -$$

$$-F_2 R_2' \left[\frac{-8}{6c} \ln \frac{(-x_1^* \cos\theta^* + \sqrt{R_2^2 + x_1^{*2}\cos^2\theta^*})}{\mathscr{R} \quad + \sqrt{R_2^2 + \mathscr{R}^2}} - \frac{8}{cR_2^2}\left(\frac{3}{4} c \sec\theta^* - \frac{x_1^*}{2}\cos\theta^*\right) \times \right.$$

$$\times \sqrt{R_2^2 + x_1^{*2}\sin^2\theta^*} + \frac{\cos\theta^* \left(\frac{-9}{8} x_1^* c^2 \sec^2\theta^* + \frac{3}{4} R_2^2 c \sec^2\theta^* + \frac{9}{4} x_1^{*2} c - x_1^{*3} \cos^2\theta^*\right)}{2\sqrt{R_2^2 + \mathscr{R}^2}} +$$

$$\left. + \frac{3}{4} \frac{c \sec^2\theta^*}{R_2^2}\left(\frac{\mathscr{R}}{\sqrt{R_2^2 + \mathscr{R}}} - \cos\theta^*\right)\right]\Bigg\} \tag{A6}$$

where

$$\mathscr{R} = \frac{3}{4} c \sec\theta^* - x_1^* \cos\theta^* \tag{A7}$$

$$R_1 = \sqrt{(x_1^* \tan\theta^* + y_1^*)^2 + (z_1^* - \tau)^2} \tag{A8}$$

$$R_2 = \sqrt{(x_1^* \tan\theta^* + y_1^*)^2 + (z_1 + \tau)^2} \tag{A9}$$

$$R_1' = (R_1 - x_1^* \sec\theta^* \tan\bar{\omega}) \cos\bar{\omega} \tag{A10}$$

$$R_2' = (R_2 - x_1^* \sec\theta^* \tan\bar{\omega}) \cos\bar{\omega} \tag{A11}$$

$$F_1 = \frac{(x_1^* \sec\theta^* + R_1' \tan\bar{\omega}) \cos\bar{\omega} \sin\theta^* + y_1^*}{R_1'} \tag{A12}$$

$$F_2 = \frac{(x_1^* \sec\theta^* + R_2' \tan\bar{\omega}) \cos\bar{\omega} \sin\theta^* + y_1^*}{R_2'} \tag{A13}$$

A.2. *Blade Pressure Distribution.*

Following Yakoyama[12] the pressure distribution on the blade surface may be determined from the relation.

$$C_p = (C_p)_{2d} - \left(\frac{w}{U_1}\right)^2 \tag{A14}$$

APPENDIX B

Theoretical Prediction of Outlet Angles.

B.1. *Change in Outlet Angle Due to Secondary Flow.*

Louis[10], in investigating secondary flow, in the presence of a wake at midspan, has demonstrated the importance of viscous effects occurring within the cascade.

Louis's expressions for the components of outlet vorticity (normal and streamwise respectively) are,

$$\Omega = \frac{\partial U}{\partial z} - \frac{1}{Uq}\int_0^x U \frac{\partial U}{\partial z}\frac{\partial q}{\partial x}\,dx - \frac{\left[U\frac{\partial}{\partial x}(qw)\right]}{Uq}x = o \tag{B1}$$

$$\xi_s = q\int_0^\varepsilon \frac{2}{q}\frac{\partial U}{\partial z}\,d\varepsilon - 2q\int_0^\varepsilon \frac{d\varepsilon}{Uq^2}\left[\int_0^x U\frac{\partial U}{\partial z}\frac{\partial q}{\partial x}\,dx\right] \tag{B2}$$

Where x = co-ordinate along the streamline

w = spanwise component of velocity

q = scalar of velocity at any point in potential flow

ε = turning angle

U = velocity derived from Schichting's wake law[17].

The integrations in equation B2 were carried out graphically. If ξ_s is known at outlet the change in outlet angle due to secondary flow $(\Delta\alpha_2)_s$ can be calculated.

B.2. *Change in Outlet Angle Due to Leakage Flow.*

An attempt has been made to predict the change in outlet angle caused by leakage flow $(\Delta\alpha_2)_c$. Because of the various assumptions made the analysis is qualitative. It is assumed, in carrying out the analysis, that

(1) The flow is steady, inviscid, and incompressible.

(2) The strength of the shed vortex at the tip is $(1-K)\Gamma_{2d}$ (where K = fraction of lift retained at the tip). This vortex is distributed over an area $(s \times \delta)$ as shown in Fig. 6, such that the strength of the vortices across the passage at any spanwise position is constant. Also, the strength of these vortices is assumed to vary sinusoidally along the span at any passage position, its values being zero at $Z = 0$ and δ, and maximum at $Z = \delta/2$.

Referring to Fig. 6, the strength of vortices along CD is constant and the distribution of vortices along AB is given,

$$\xi_c = (\xi_c)_{\max} \sin \pi Z/\delta. \tag{B3}$$

This implies that $\xi_c = 0$ when $Z = 0$ and δ

$$\xi_c = (\xi_c)_{\max} \text{when } Z = \delta/2.$$

The secondary velocities induced by leakage vortices may be represented by a stream function ψ_c given by

$$\nabla^2 \psi_c = \xi_c = (\xi_c)_{\max} \sin \pi Z/\delta \tag{B4}$$

$\psi = 0$ for $Y = 0$ and s', $Z = 0$ and δ and outside the boundary layer,

$$\nabla^2 \psi_c = 0. \tag{B5}$$

Proceeding on the same lines as Hawthorne[6], by assuming an expression for ξ, given by

$$\xi_c = \sin\frac{\pi Z}{\delta} \sum_{n=1,3,5}^{\infty} \frac{4(\xi_c)_{\max}}{n\pi} \sin(n\pi Y/s') \tag{B6}$$

and considering a solution for ψ_c in the form,

$$\psi_c = \sum_{n=1,3,5}^{\infty} \psi_n(Z). \sin(n\pi Y/s') \tag{B7}$$

it can be proved that

$$\psi_n = \frac{-4(\xi_c)_{\max} s'}{(n\pi)^2} \left\{ \frac{\sinh n\pi \frac{Z}{s'}}{\sinh n\frac{\pi l}{s'}} \int_Z^l \sin\frac{\pi Z}{\delta} \sinh\frac{n\pi(l-Z)}{s'} dZ \right.$$

$$\left. + \frac{\sinh \frac{n\pi}{s'}(l-Z)}{\sinh \frac{n\pi l}{s'}} \int_0^Z \sin\frac{\pi Z}{\delta} . \sinh\frac{n\pi Z}{s'} dZ \right\}. \tag{B8}$$

$$\frac{\partial\psi}{\partial Z} = \psi_n' = \frac{-4(\xi_c)_{\max}}{n\pi} \left\{ \frac{\cosh\frac{n\pi Z}{s'}}{\sinh\frac{n\pi l}{s}} \int_z^l \sin\frac{\pi Z}{\delta} . \sinh\frac{n\pi(l-Z)}{s'} . dZ - \right.$$

$$\left. - \frac{\cosh n\pi\frac{(l-Z)}{s'}}{\sinh\frac{n\pi l}{s'}} \int_0^Z \sin\frac{\pi Z}{\delta} \sinh\frac{n\pi Z}{s'} dZ \right\}. \tag{B9}$$

By using the general formula for integration by parts and after further simplification, it can be proved that

For $0 \leqslant Z \leqslant \delta$

$$\psi_n = \frac{-4(\xi_c)_{\max} . s' . \delta}{(n\pi)^2\pi \left[1 + \left(n\frac{\delta}{s'}\right)^2\right]} \left\{ \left[\frac{n\delta}{S'} \sin\frac{\pi Z}{\delta}\right] + \left[\frac{\sinh\frac{n\pi(l-\delta)}{s'}}{\sinh\frac{n\pi l}{s'}} . \sinh\left(\frac{n\pi\delta}{s'} . Z/\delta\right)\right] \right\} \tag{B10}$$

and

$$\psi'_n = \frac{-4(\xi_c)_{\max}.\,\delta}{n\pi^2\left[1+\left(n\frac{\delta}{s'}\right)^2\right]}\left\{\left[\cos\frac{\pi Z}{\delta}\right]+\left[\frac{\sinh\frac{n\pi(l-\delta)}{S'}}{\sinh\frac{n\pi l}{s'}}\cosh\left(\frac{n\pi\delta}{s'}.\,Z/\delta\right)\right]\right\}. \tag{B11}$$

For $\delta \leqslant Z \leqslant l$

$$\psi_n = \frac{-4(\xi_c)_{\max}.\,s'.\,\delta}{(n\pi)^2\pi\left[1+\left(n\frac{\delta}{s'}\right)^2\right]}\left\{\frac{\sinh\frac{n\pi\delta}{s'}}{\sinh\frac{n\pi l}{s'}}.\sinh\frac{n\pi l}{s'}(1-Z/l)\right\}. \tag{B12}$$

$$\psi'_n = \frac{-4(\xi_c)_{\max}\,\delta}{n\pi^2\left[1+\left(n\frac{\delta}{s'}\right)^2\right]}\left\{\frac{\sinh.\frac{n\pi\delta}{s'}}{\sinh\frac{n\pi l}{s'}}\cosh\left[\frac{n\pi l}{s'}(1-Z/l)\right]\right\}. \tag{B13}$$

Knowing ψ_n and ψ'_n at any position, the change in outlet angle due to leakage flow $(\Delta\bar{\alpha}_2)_c$ can be calculated from the equation

$$(\Delta\bar{\alpha}_2)_c = \frac{2}{\pi U_2}\sum\frac{\psi'_n}{n},\ (\textit{See}\ \text{Ref. 6})$$

B.2. *Total Change in Outlet Angle Due to Both Seconary and Leakage Flows.*

The passage inside the boundary layer is filled with distributed leakage vortices of strength ξ_c and secondary vortices of strength $-\xi_s$. When mathematically represented the flow fields are respectively given by

$$\nabla^2\psi_s = -\xi_s \tag{B14}$$

and

$$\nabla^2\psi_c = \xi_c \tag{B15}$$

where ψ_s and ψ_c are stream functions due to secondary flow and leakage flow respectively.

Since the boundary conditions are the same, equations (B14) and (B15) may be added together,

$$\nabla^2(\psi_s+\psi_c) = \xi_c-\xi_s. \tag{B16}$$

Hence the solutions obtained from equations (B14) and (B15) can be added to give the total change in outlet angle,

$$\Delta\bar{\alpha}_2 = (\Delta\bar{\alpha}_2)_c+(\Delta\bar{\alpha}_2)_s. \tag{B17}$$

Values of $(\Delta\bar{\alpha}_2)_s$ can be obtained from Louis's[10] viscous theory (Section B1) and that of $(\Delta\bar{\alpha}_2)_c$ from the analysis in this Section.

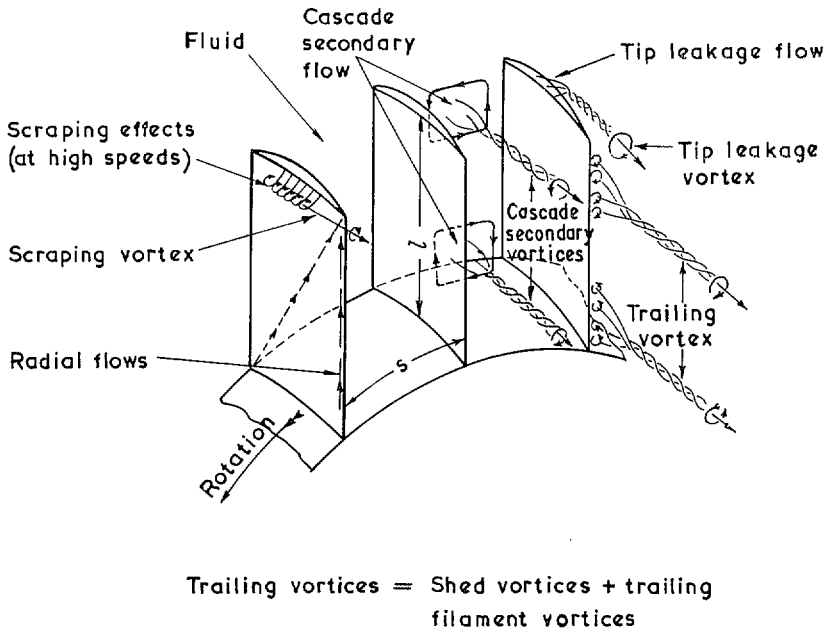

FIG. 1. Secondary flow and vortices in an axial flow compressor rotor.

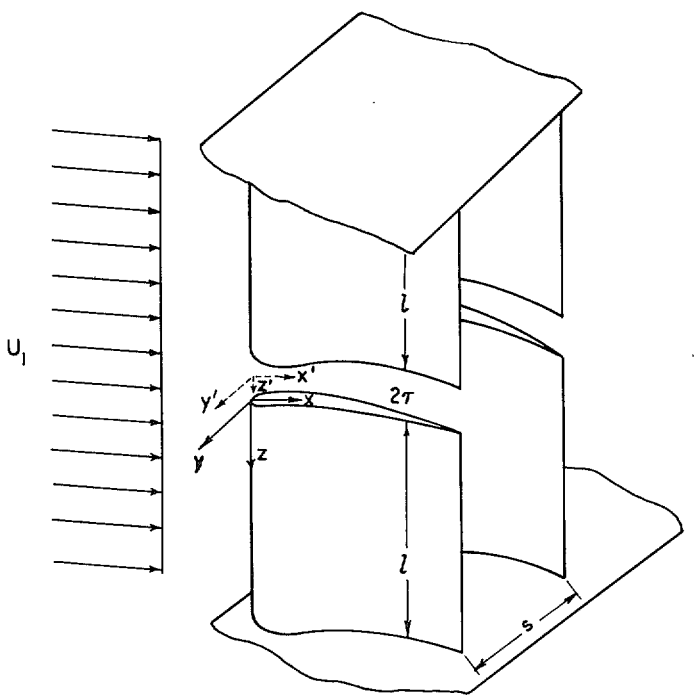

FIG. 2a. Cascade of split blades with uniform upstream flow. (Experiment A).

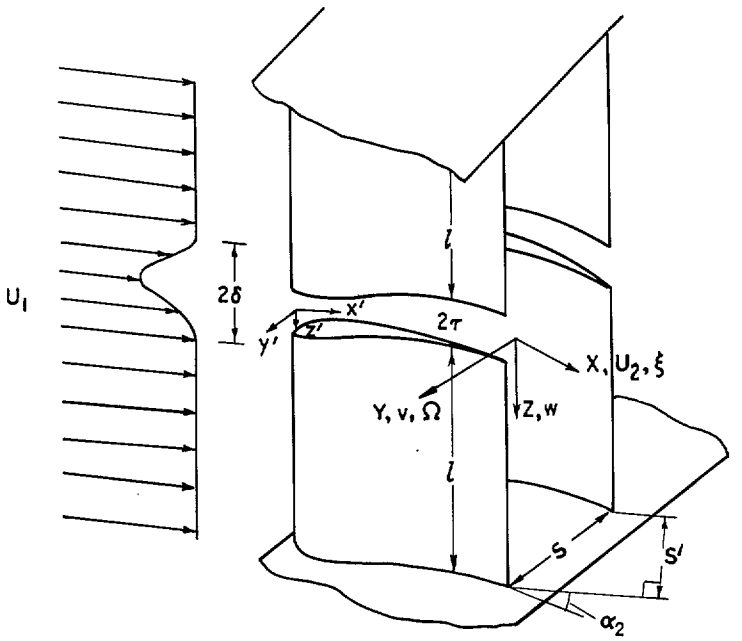

FIG. 2b. Cascade of split blades with an entry vorticity (normal component) at the tip. (Experiment B).

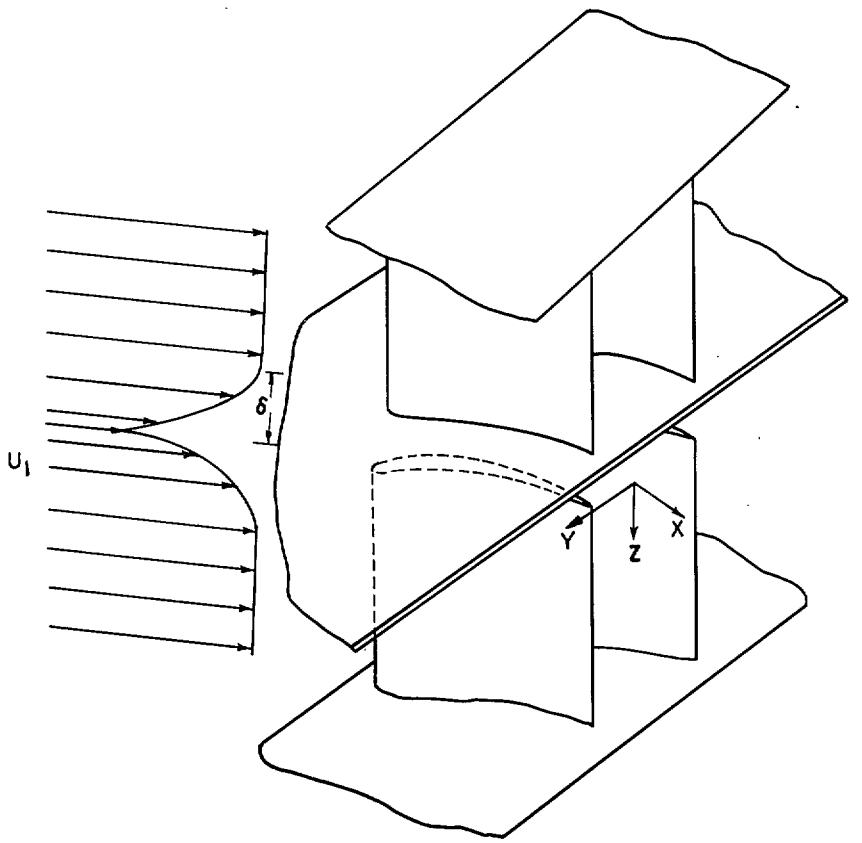

FIG. 2c. Cascade of split blades with an end wall and steep entry velocity gradient at the tip. (Experiment C).

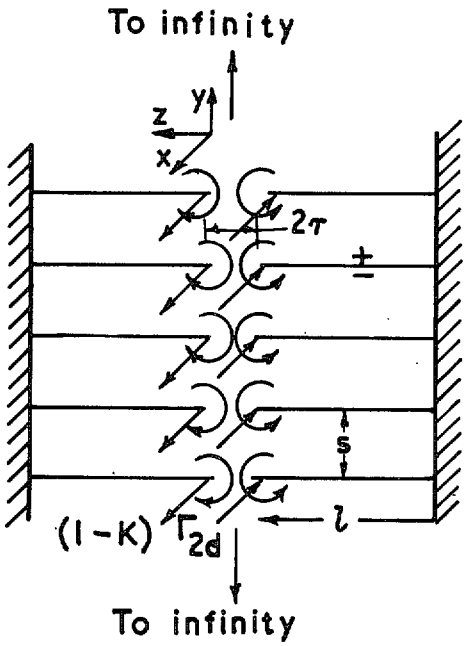

FIG. 3. Vortex system in a cascade (Experiment A) for the prediction of induced drag.

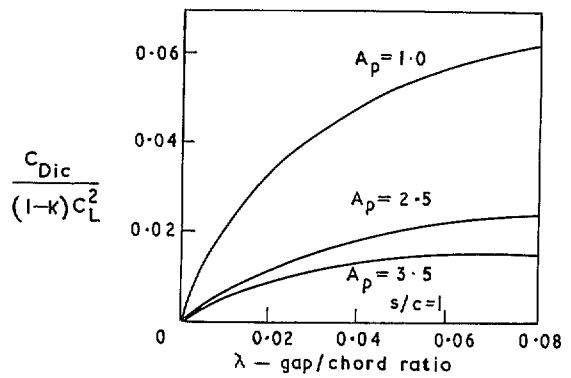

(a) Effect of passage aspect ratio

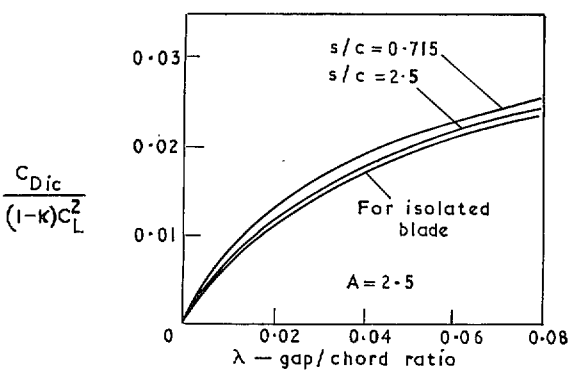

(b) Effect of space/chord ratio

FIG. 4. Effect of space/chord ratio and aspect ratio on leakage losses in a cascade with uniform upstream flow (theoretical).

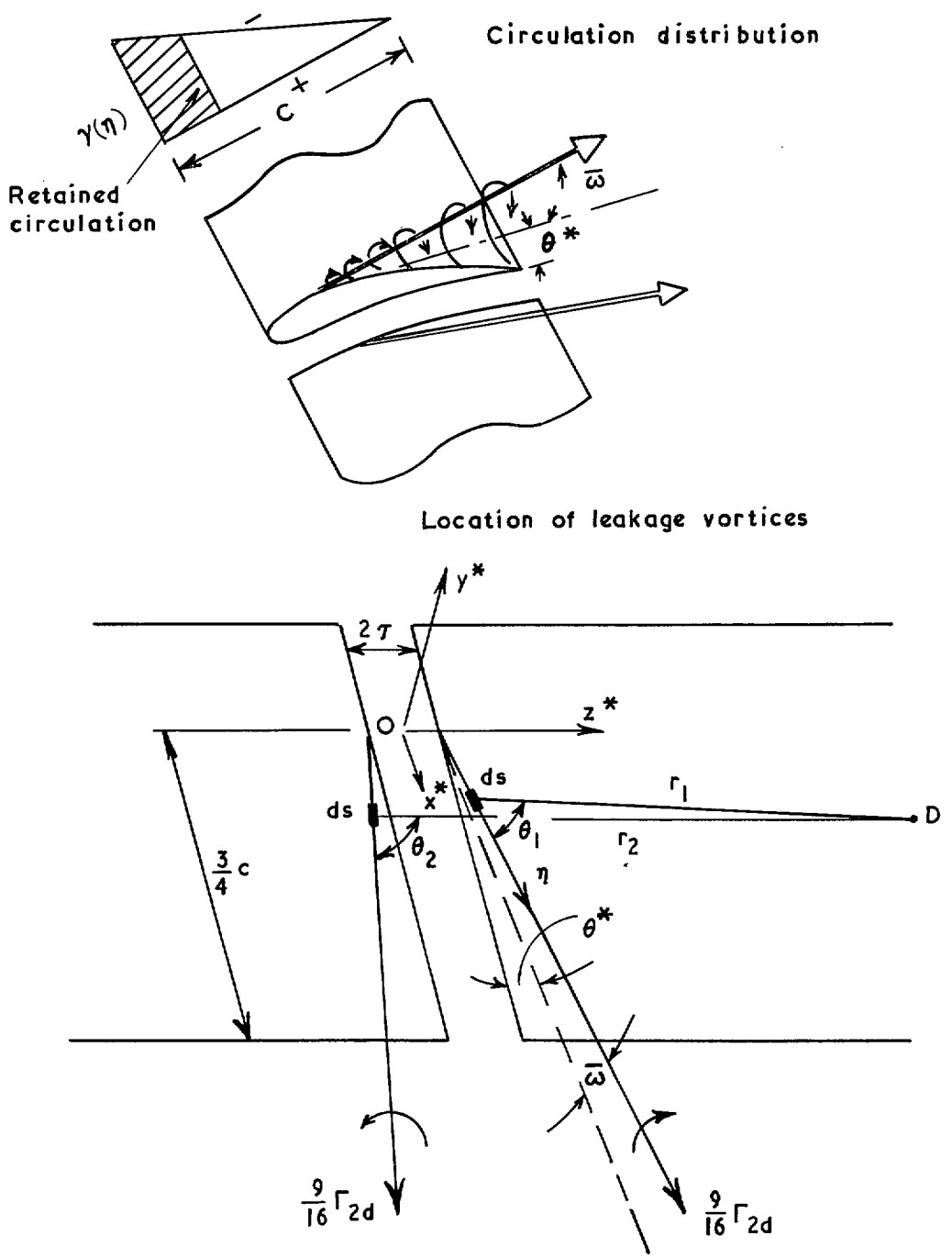

FIG. 5. Notation used for analytical prediction of pressure distribution.

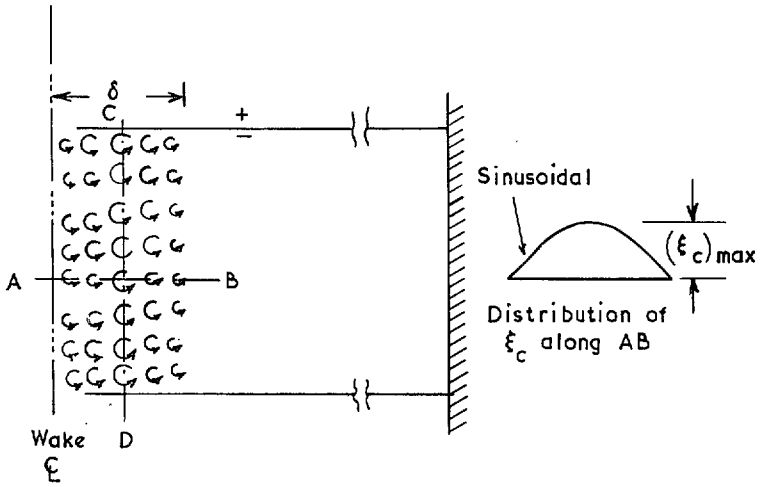

FIG. 6. Leakage vortex distribution assumed for outlet angle prediction (Appendix B).

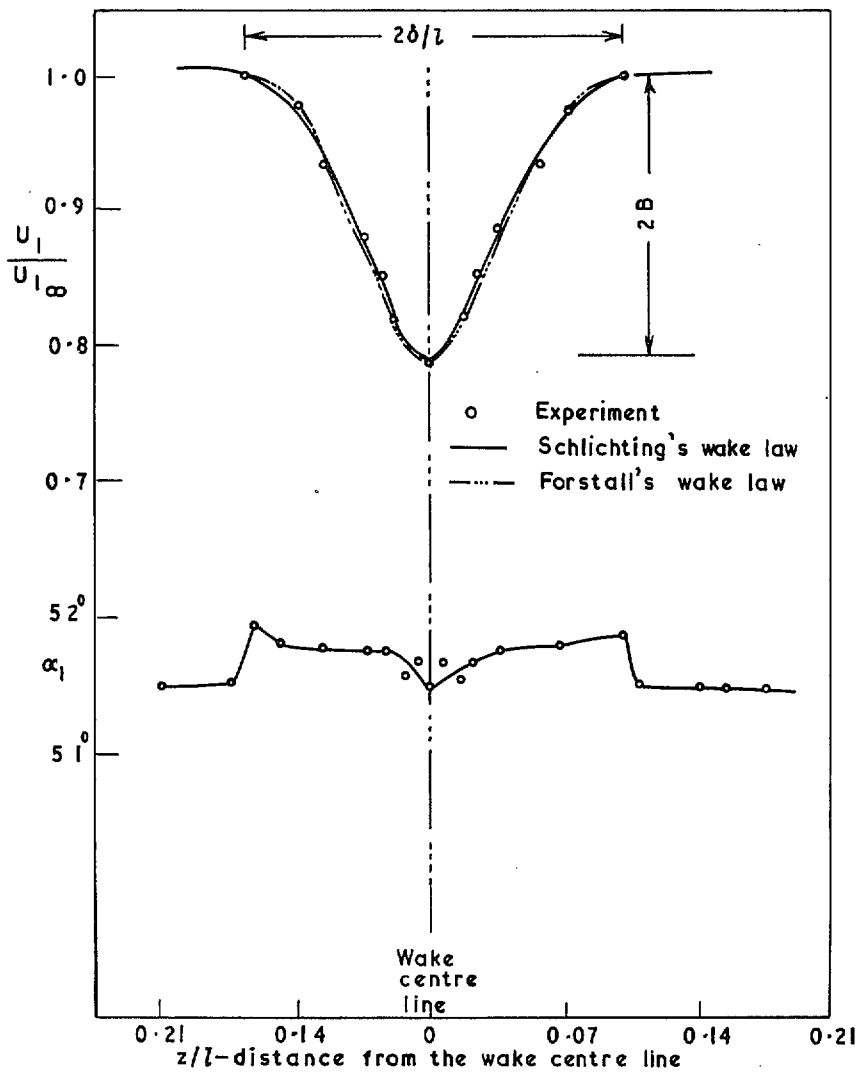

FIG. 7. Inlet velocity and outlet angle for Experiment B.

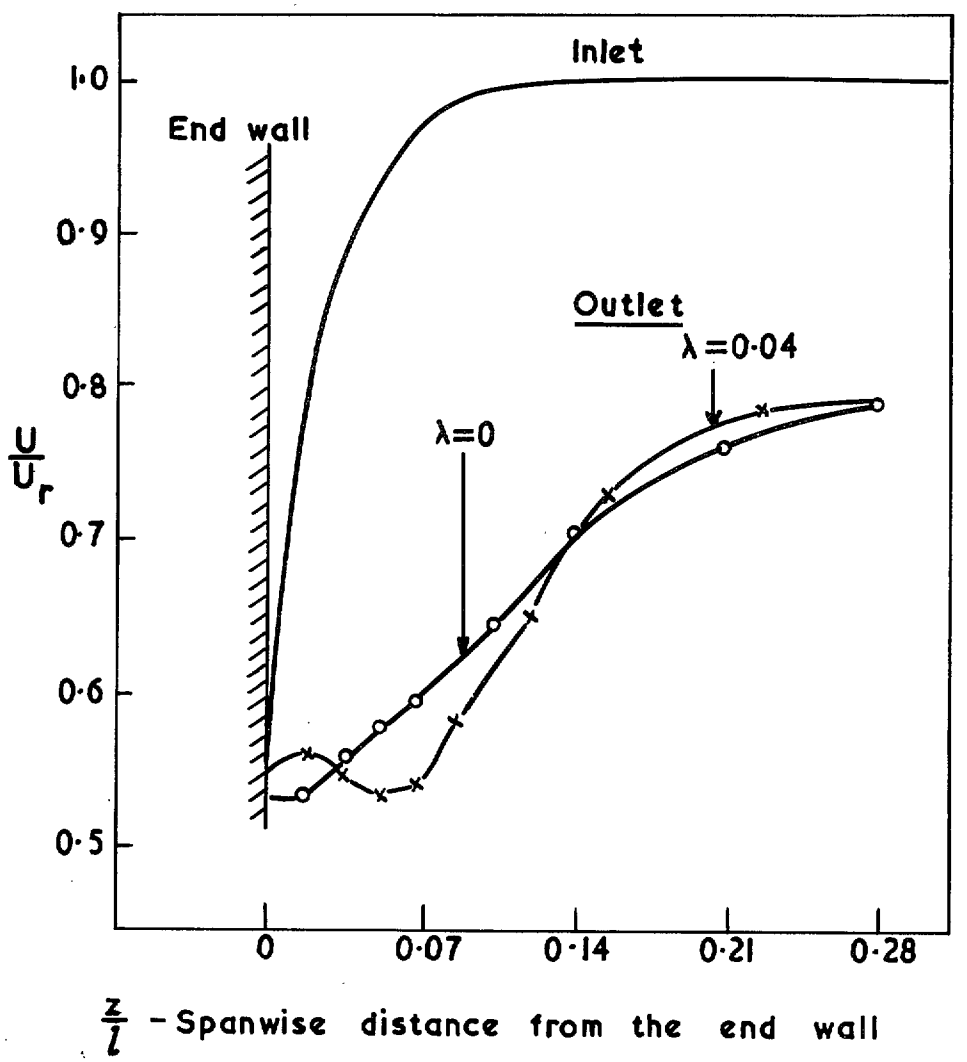

FIG. 8. Velocity profiles at inlet and outlet for $\lambda = 0$ and $\lambda = 0{\cdot}04$. (Experiment C).

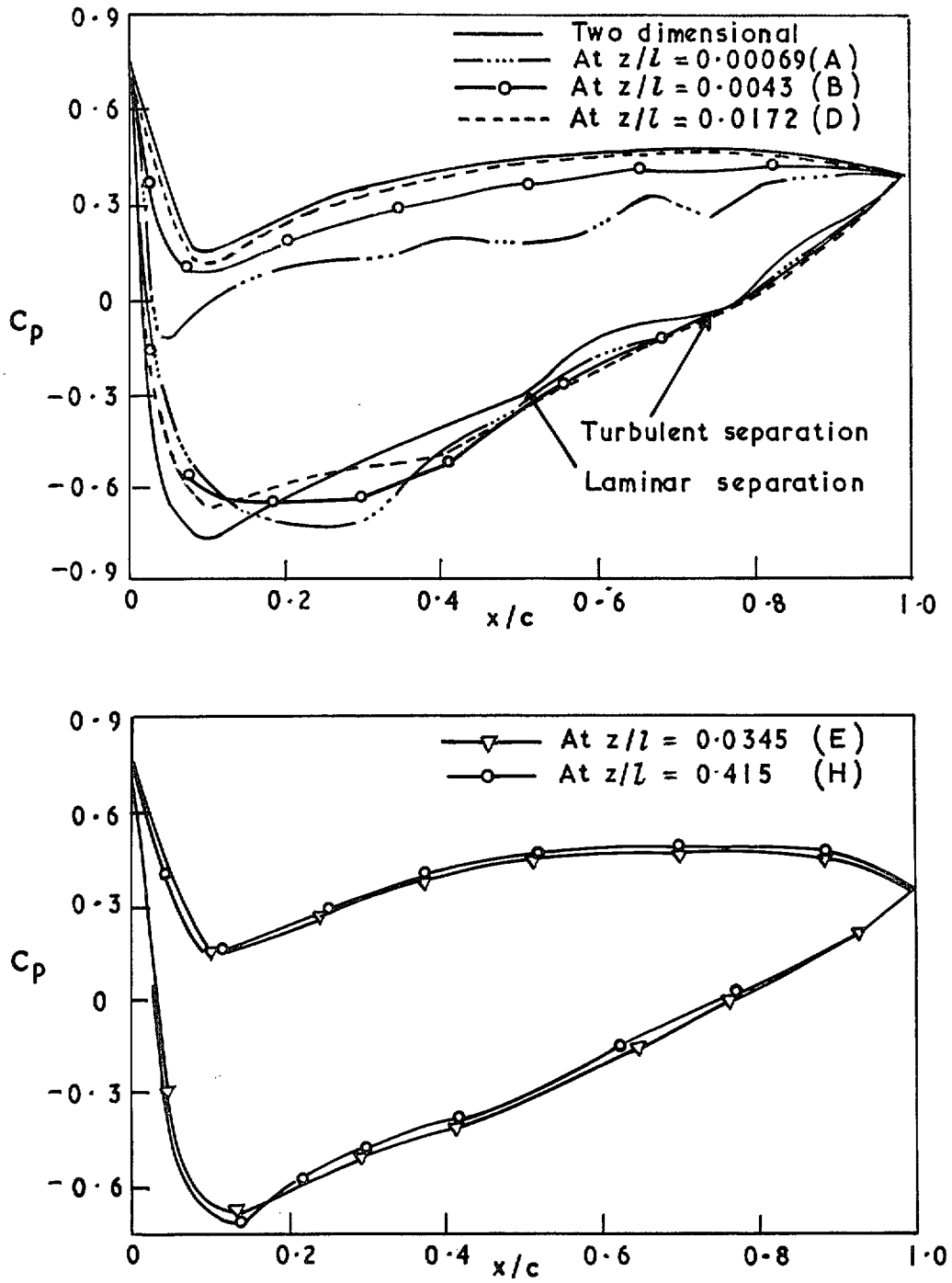

FIG. 9a. Chordwise pressure distributions at various spanwise positions for $\lambda = 0{\cdot}01$. (Experiment A).

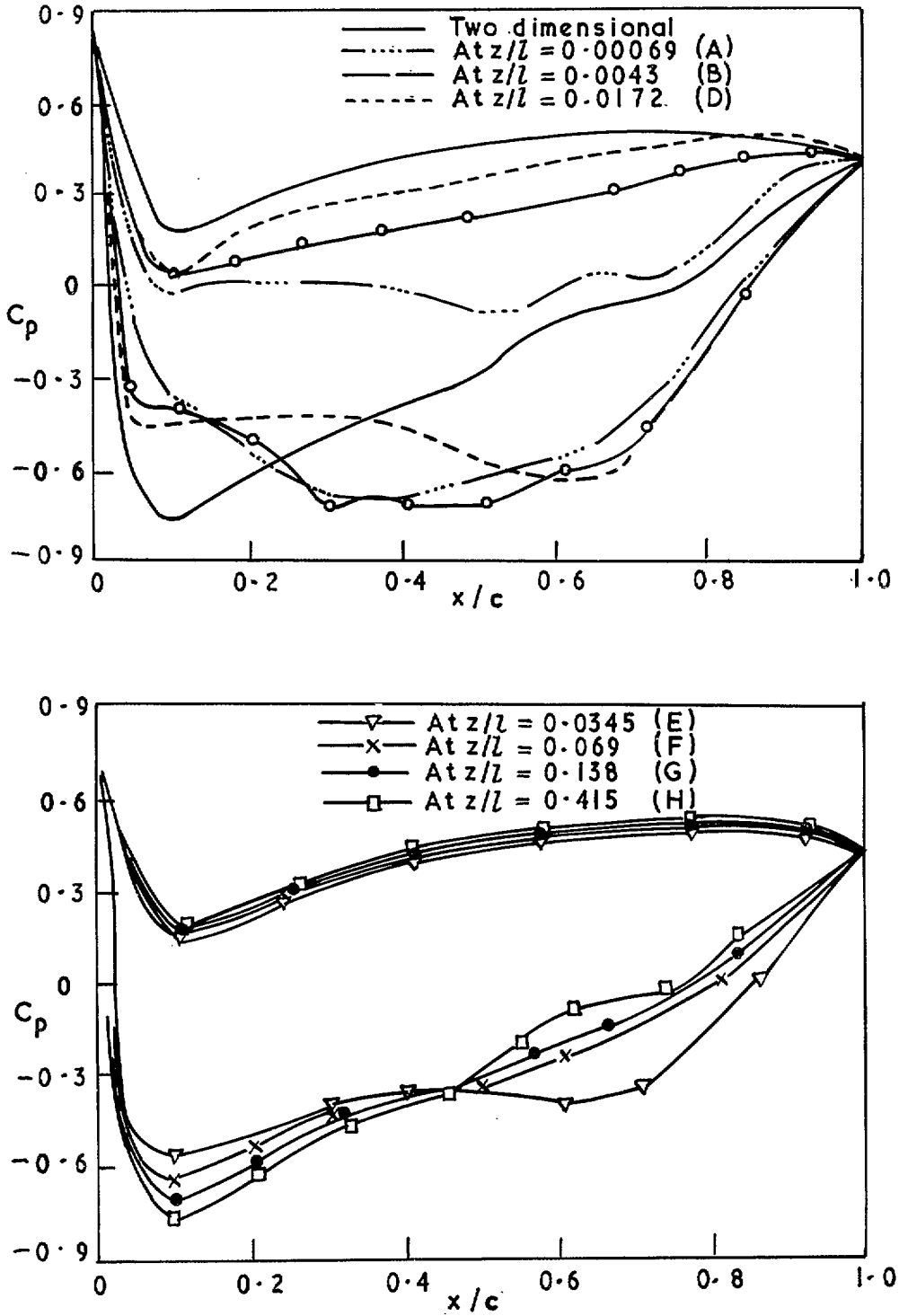

FIG. 9b. Chordwise pressure distributions at various spanwise positions for $\lambda = 0{\cdot}04$. (Experiment A).

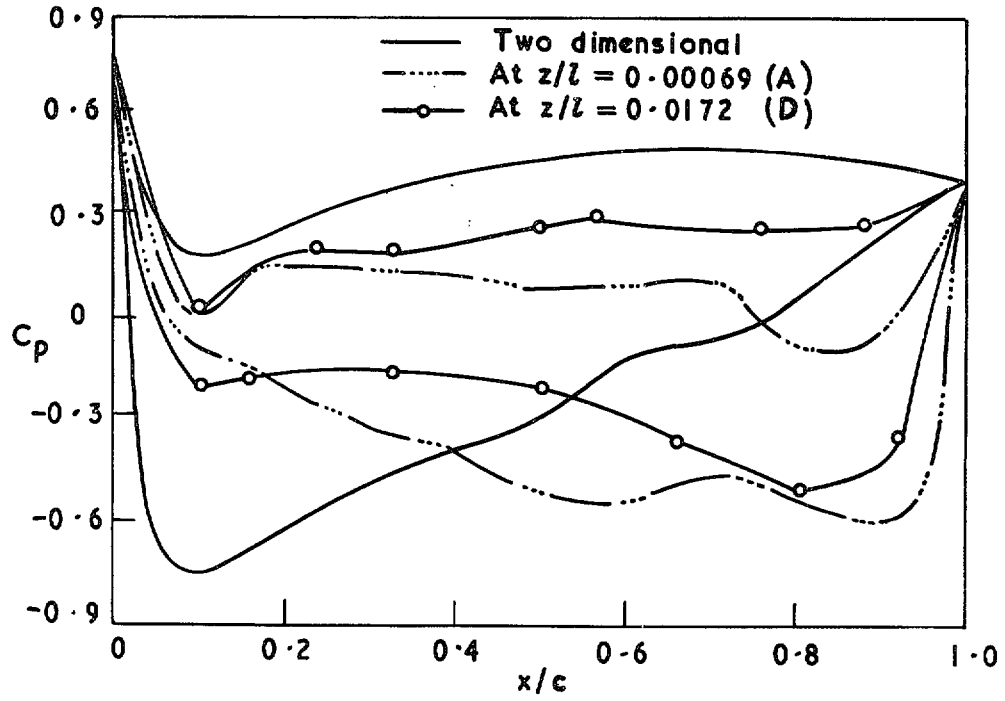

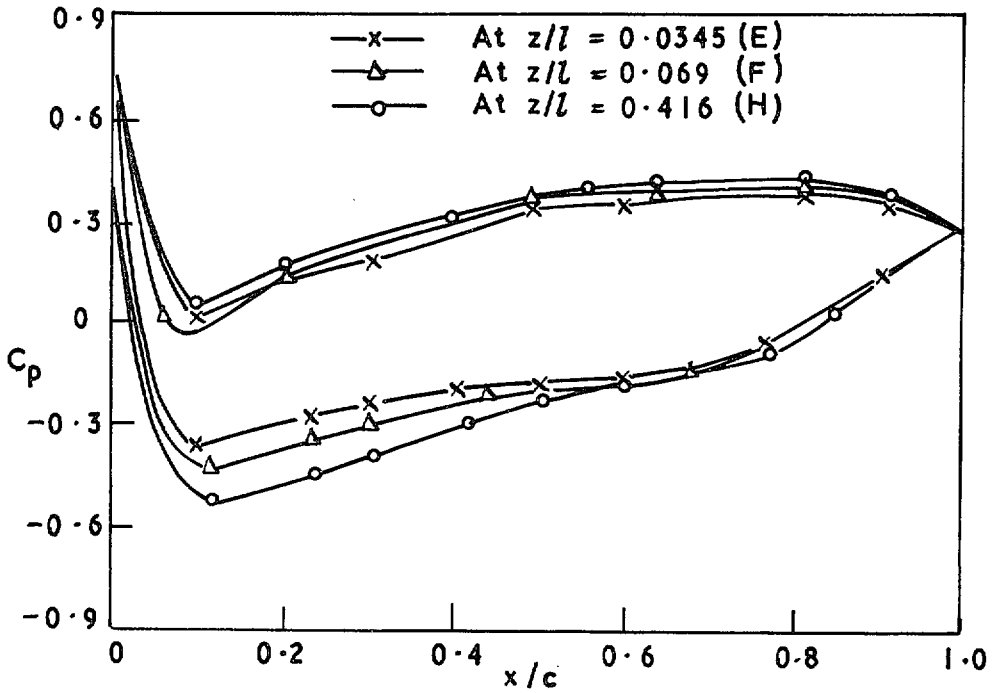

FIG. 9c. Chordwise pressure distributions at various spanwise positions for every large gap/chord ratio. (Experiment A).

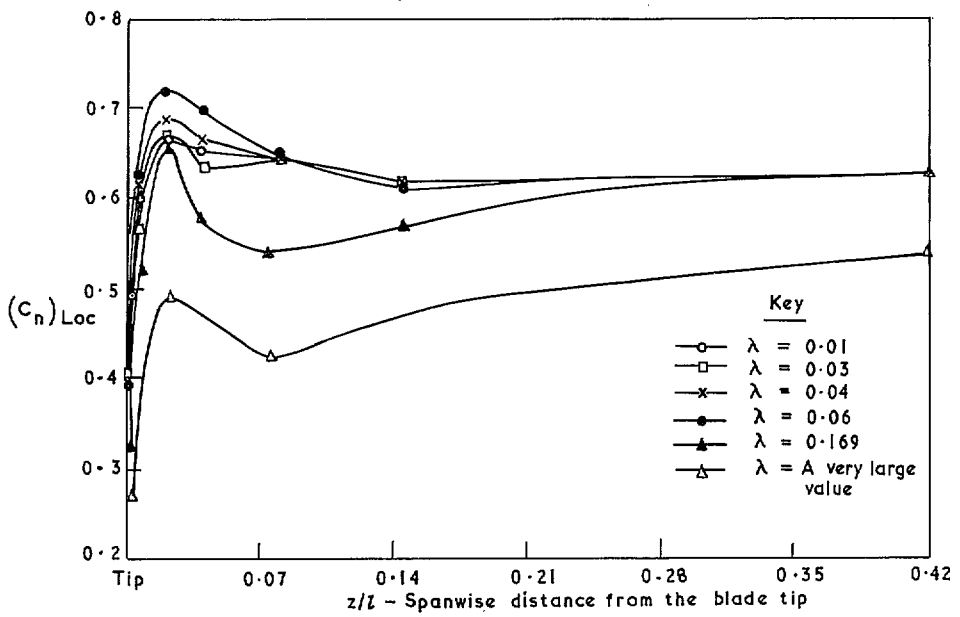

FIG. 10. Spanwise distribution of normal force coefficient for various gap/chord ratios. (Experiment A).

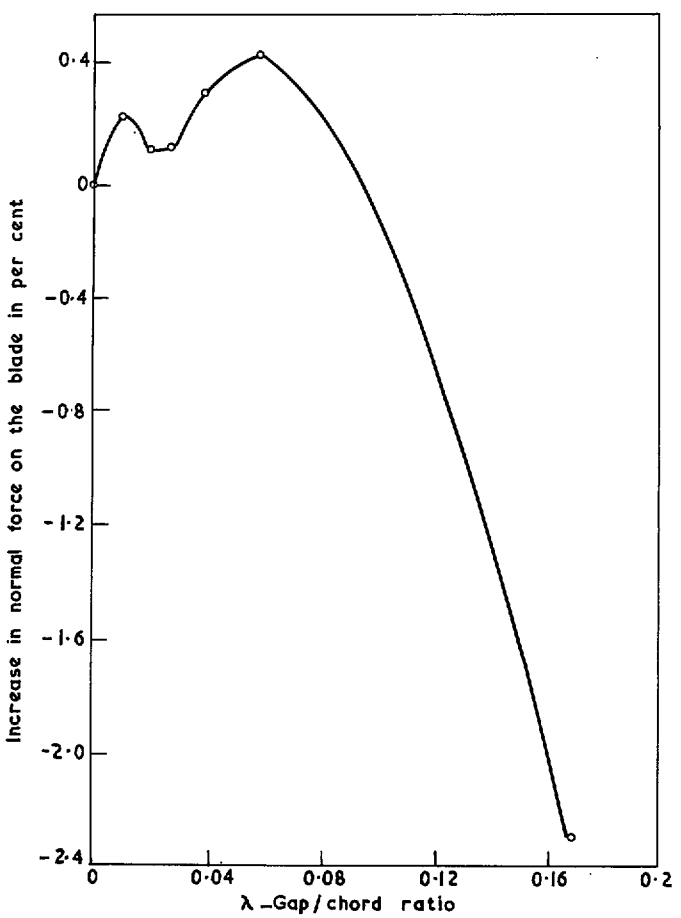

FIG. 11. Change in average normal force for various gap/chord ratios. (Experiment A).

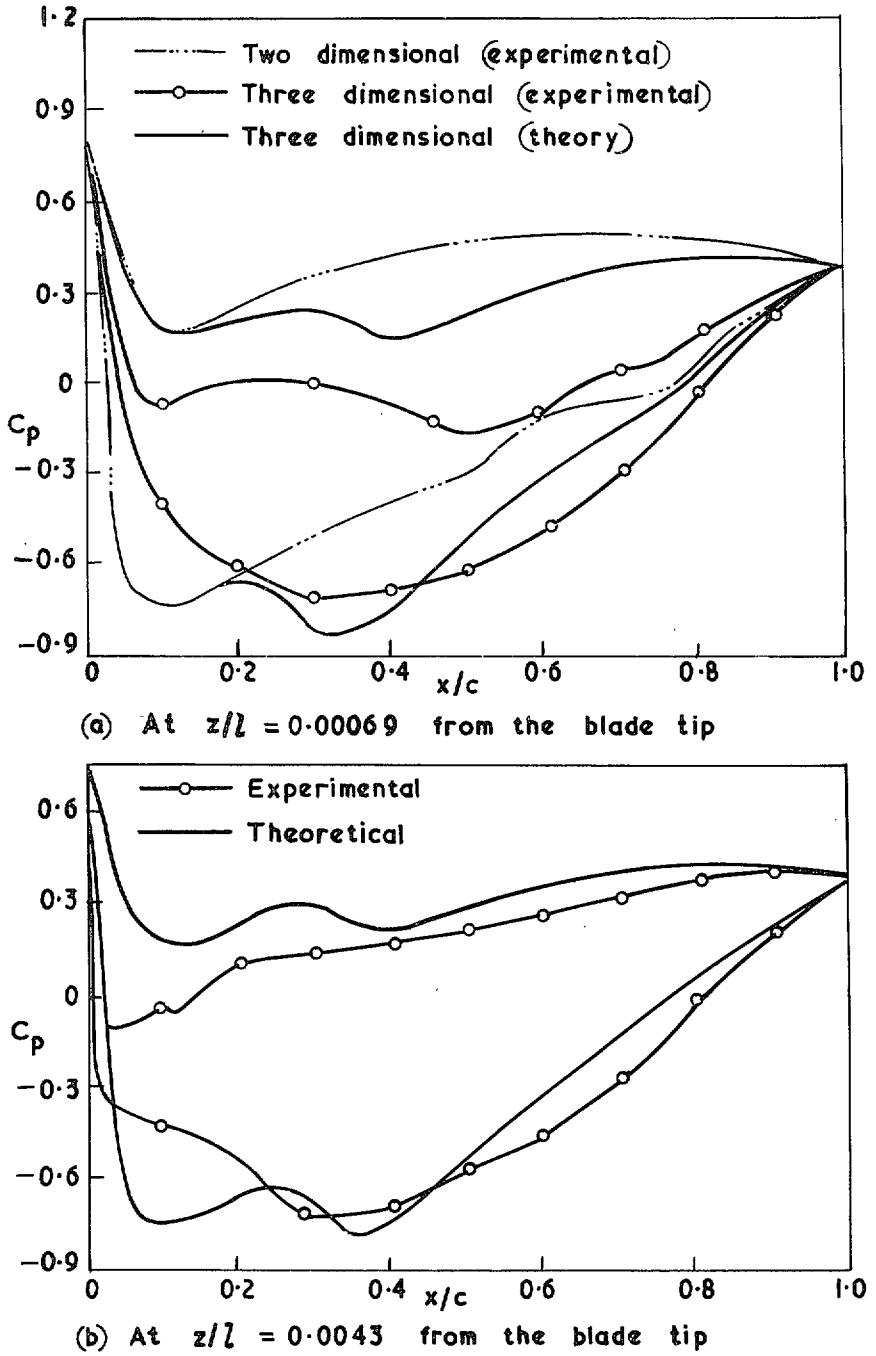

FIG. 12a & b. Comparison between theoretical and experimental chordwise pressure distributions at various spanwise positions for $\lambda = 0{\cdot}03$. (Experiment A).

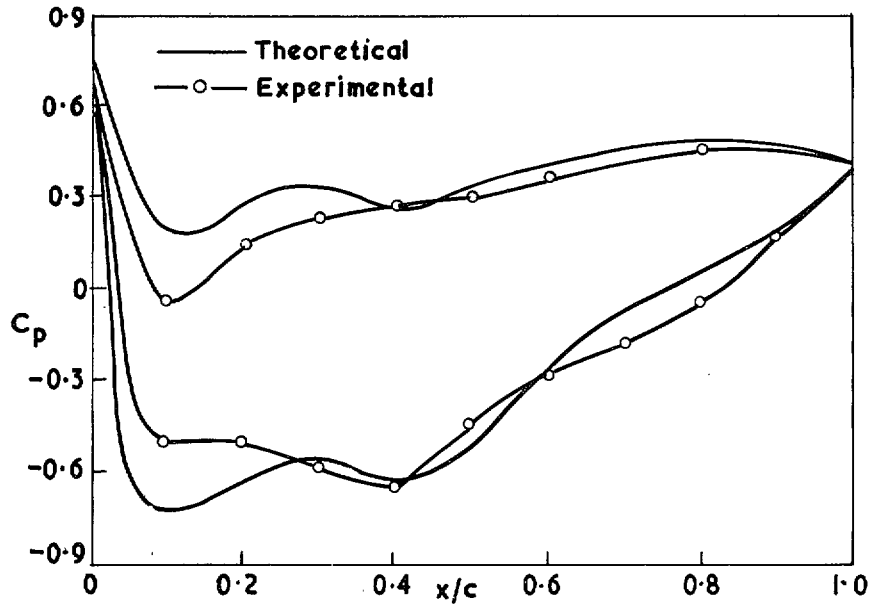

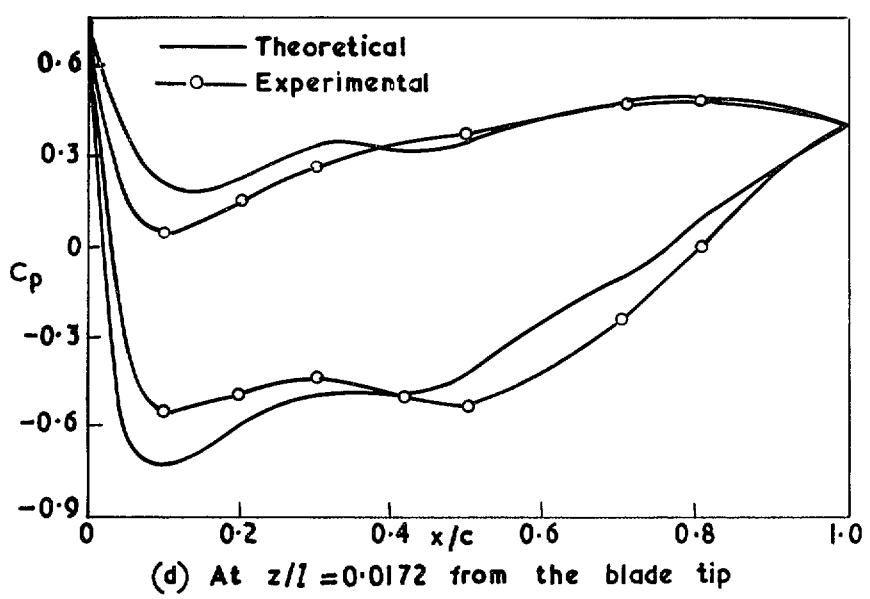

FIG. 12c & d. Comparison between theoretical and experimental chordwise pressure distributions at various spanwise positions for $\lambda = 0{\cdot}03$. (Experimental A).

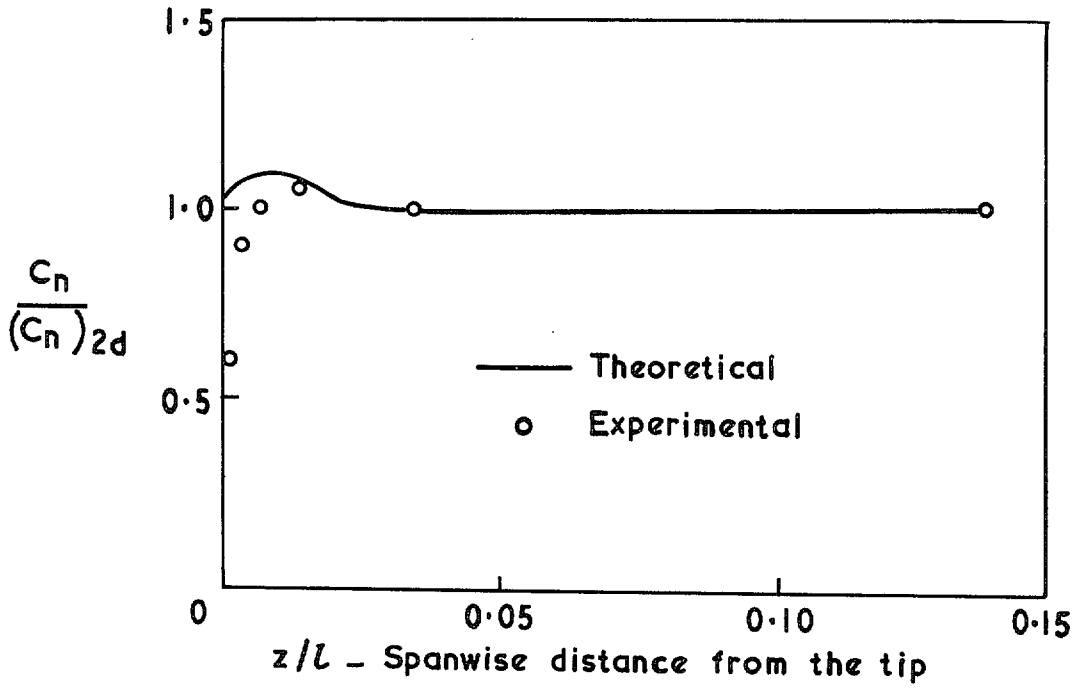

FIG. 12e. Theoretical and experimental comparison of spanwise distribution of normal force for $\lambda = 0{\cdot}03$ (Experiment A).

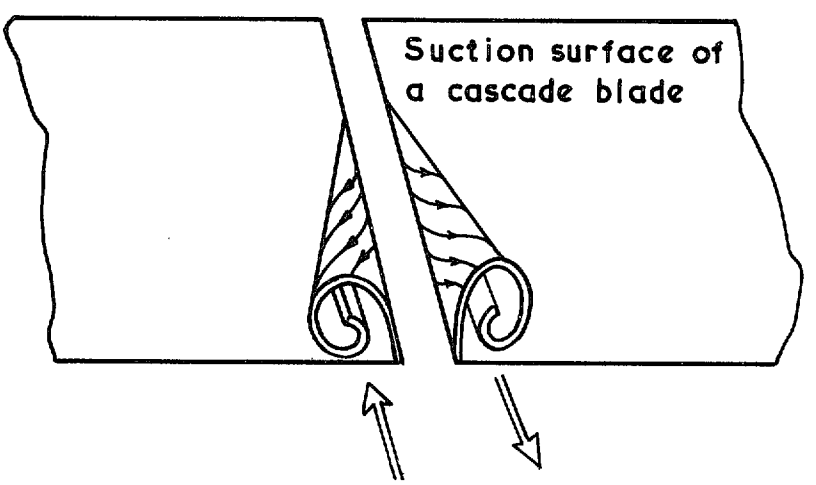

FIG. 13. The three dimensionality of the leakage vortices.

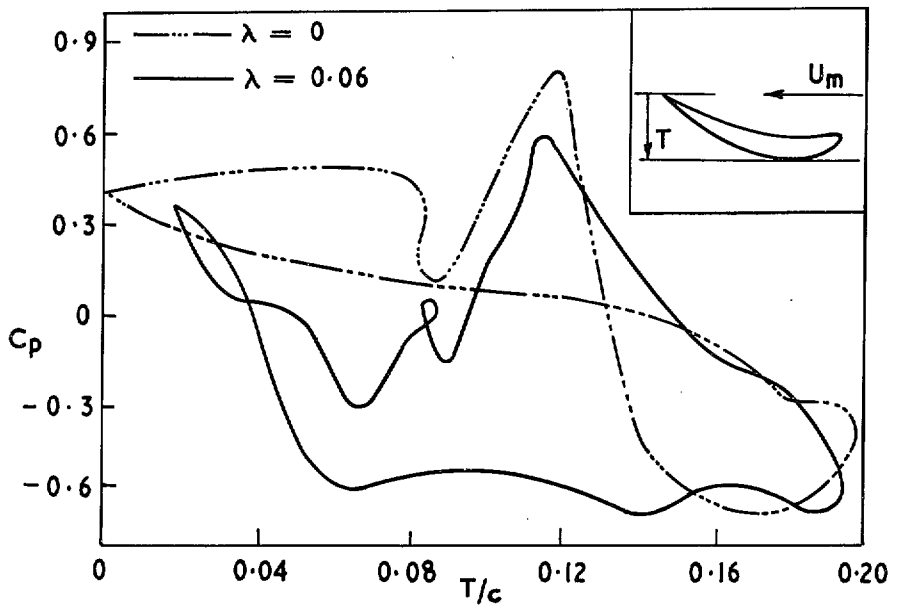

FIG. 14. Blade pressure distribution plotted perpendicular to mean stream velocity.

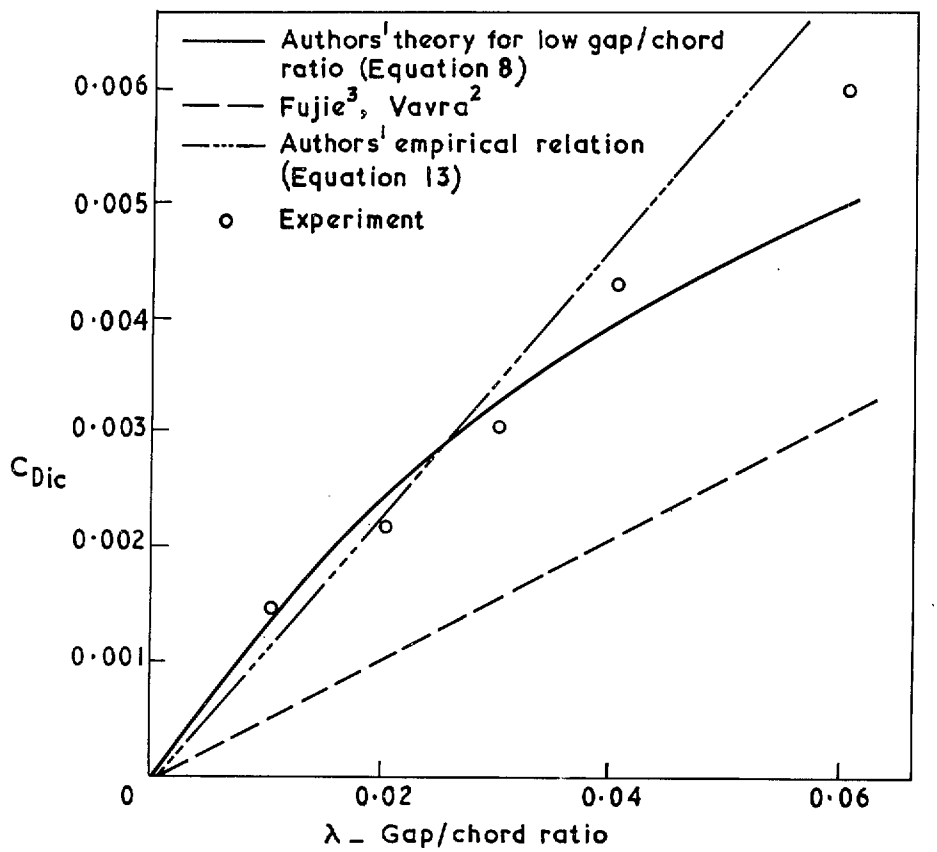

FIG. 15. Comparison between experimental and theoretical values of C_{Dic} for uniform inlet flow.

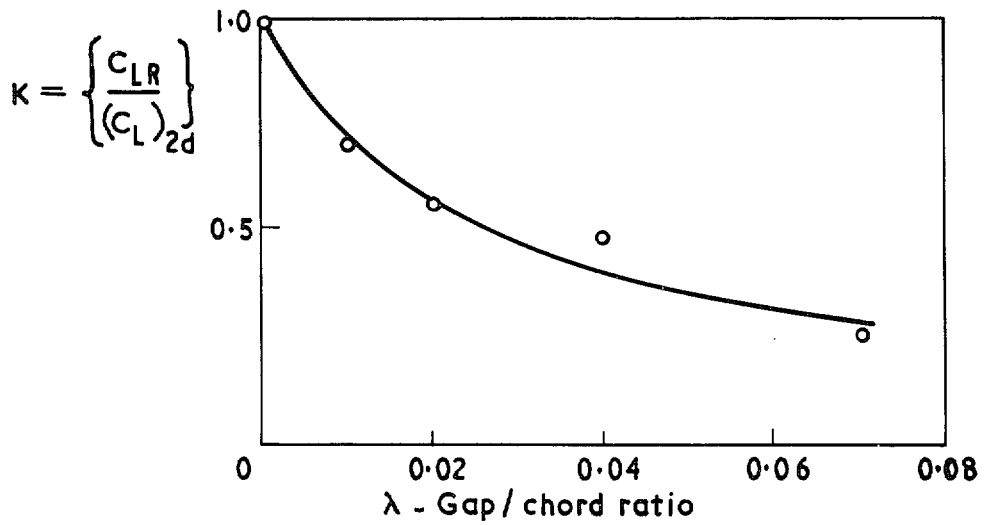

FIG. 16a. Values of lift retained (as a fraction of two dimensional value) at the tip of the cascade blade.

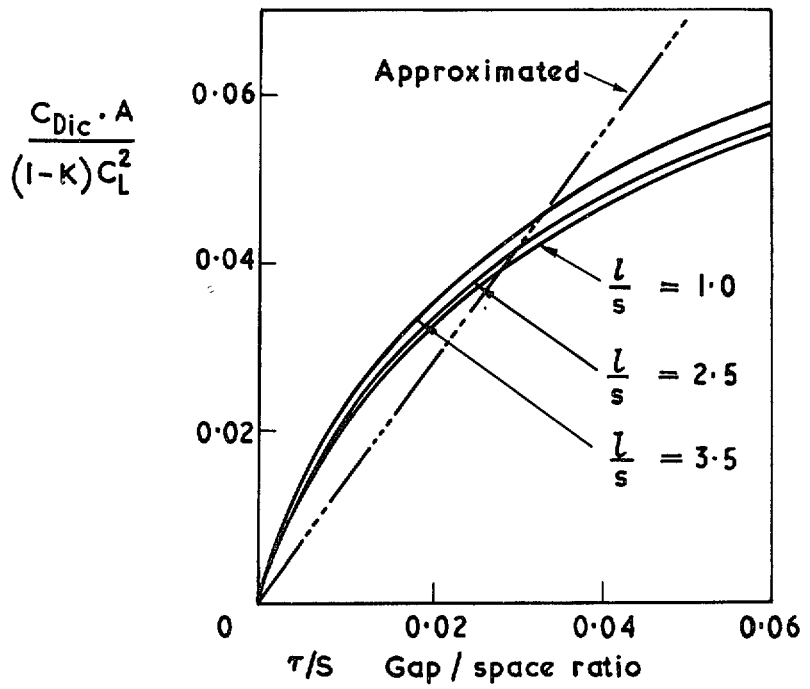

FIG. 16b. Variation of C_{Dic}, equation (8), with gap/space ratio for various values of l/s (for uniform inlet flow).

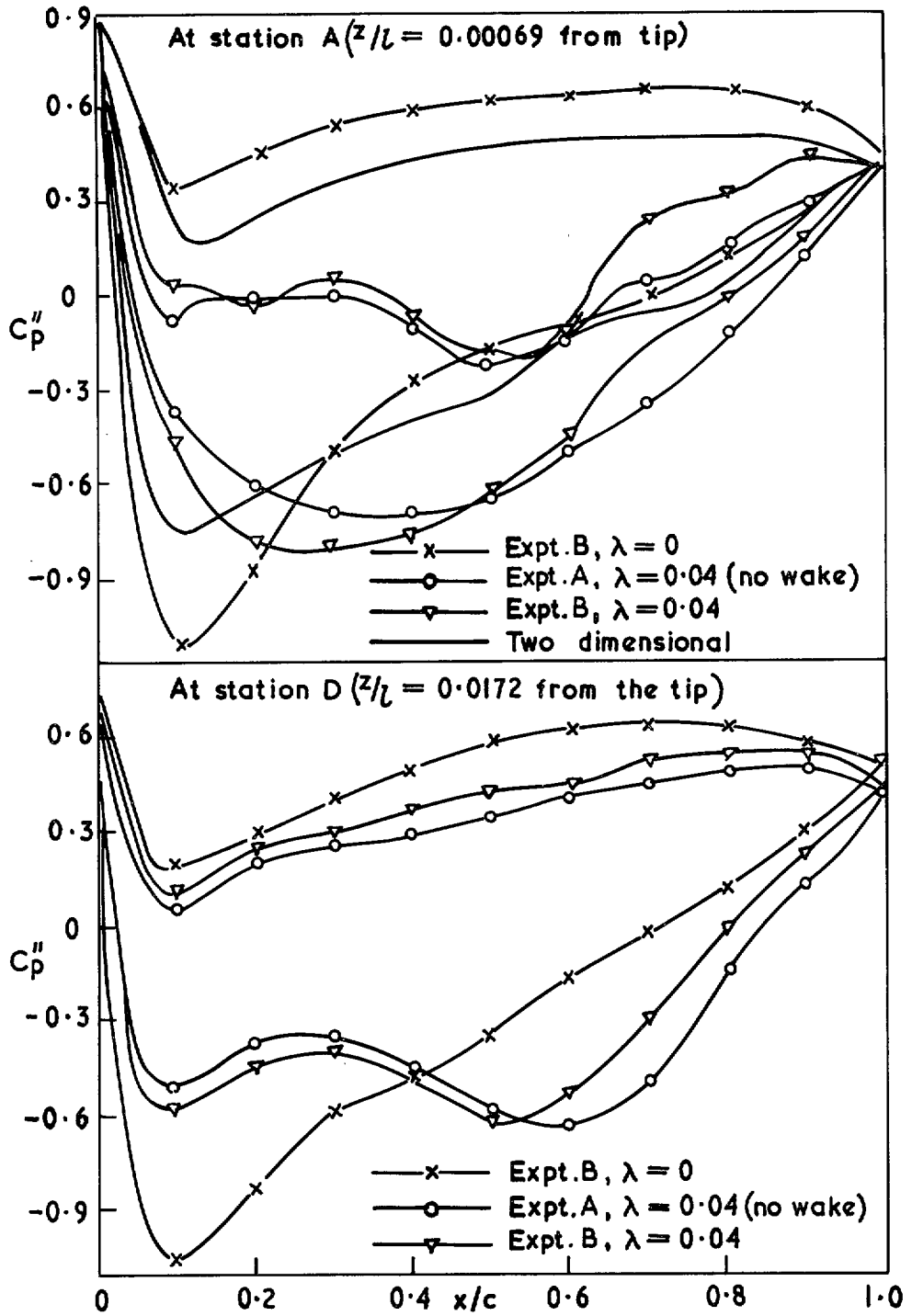

FIG. 17. Comparison of blade pressure distributions obtained for zero and 4 per cent gap/chord ratio.

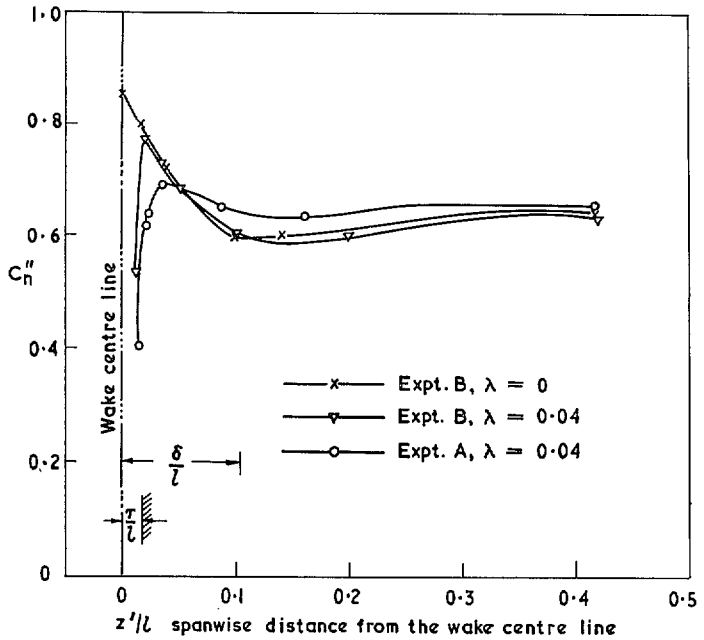

FIG. 18. Spanwise distribution of normal force coefficient for $\lambda = 0$ and 0·04. (Experiment A and B).

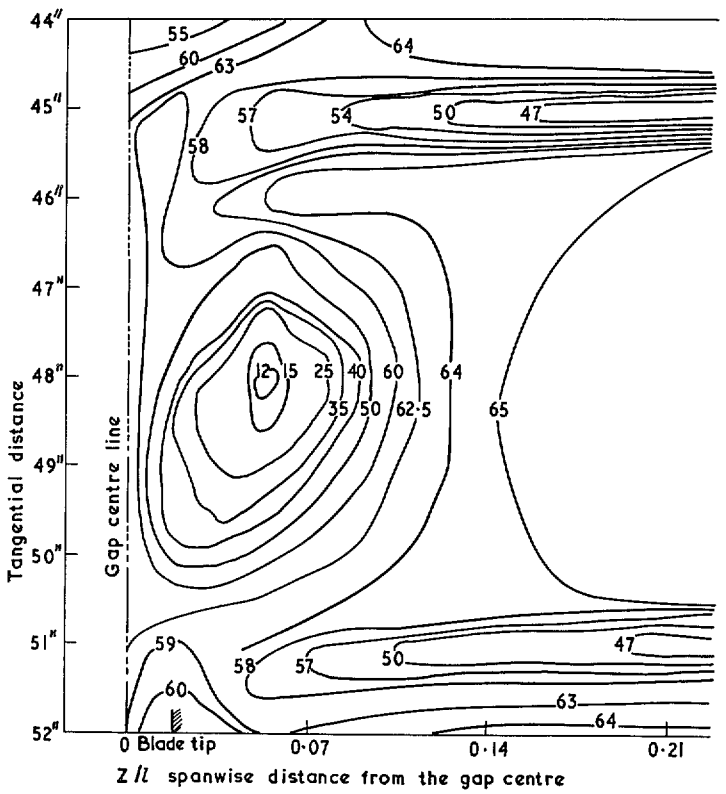

FIG. 19a. Contours of constant dynamic pressure at outlet for $\lambda = 0{\cdot}04$. (Uniform upstream flow, Experiment A).

The numbers on the contours denote the dynamic pressure at outlet as a percentage of reference dynamic pressure at inlet.

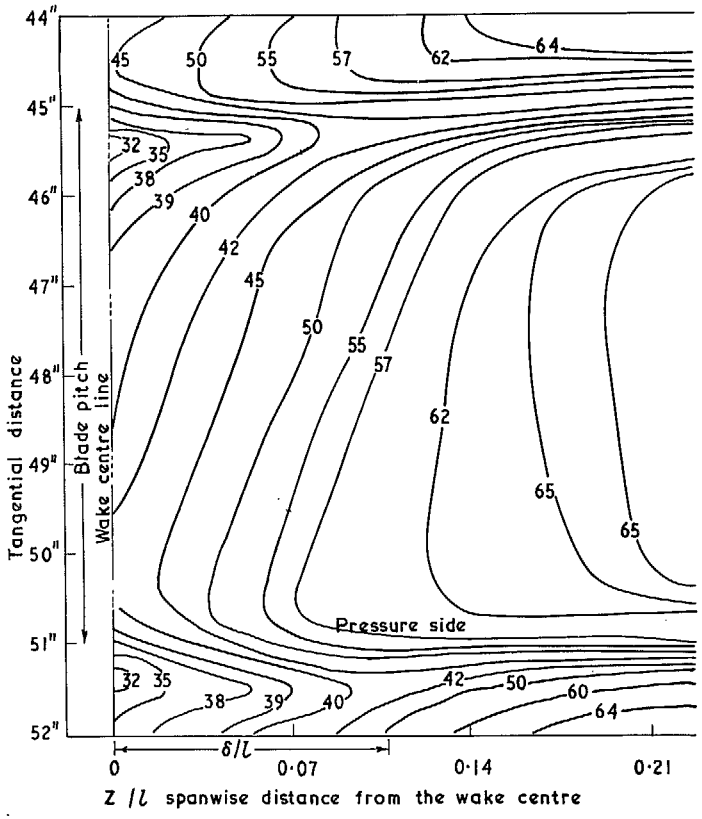

FIG. 19b. Contours of constant dynamic pressure at outlet for $\lambda = 0$ (Non-uniform upstream flow, Experiment B).

The numbers on the contours denote the dynamic pressure at outlet as a percentage of reference dynamic pressure at inlet.

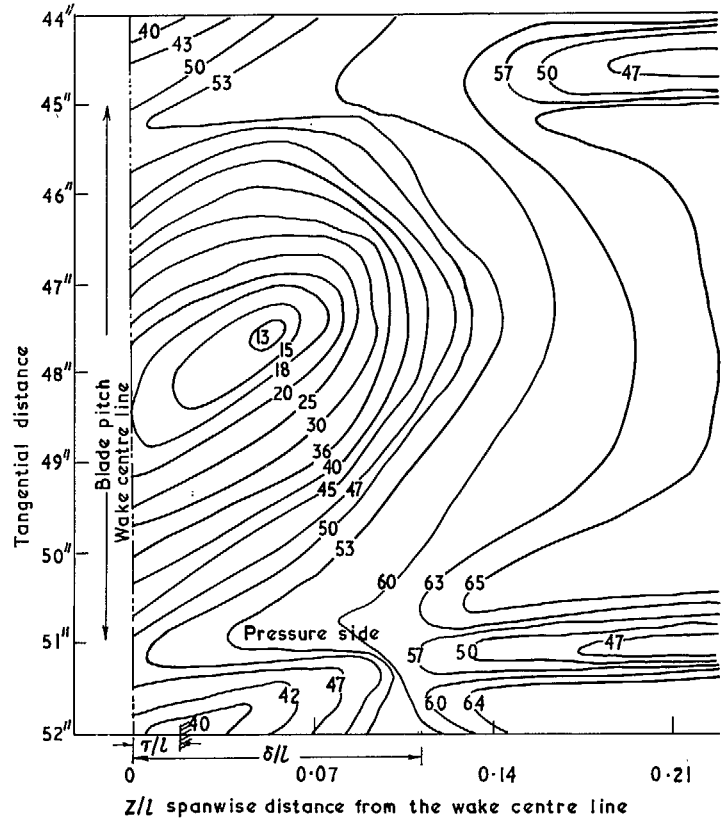

FIG. 19c. Contours of constant dynamic pressure at outlet for $\lambda = 0{\cdot}04$. (Non-uniform upstream flow, Experiment B).

The numbers on the contours denote the dynamic pressure at outlet as a percentage of reference dynamic pressure at inlet.

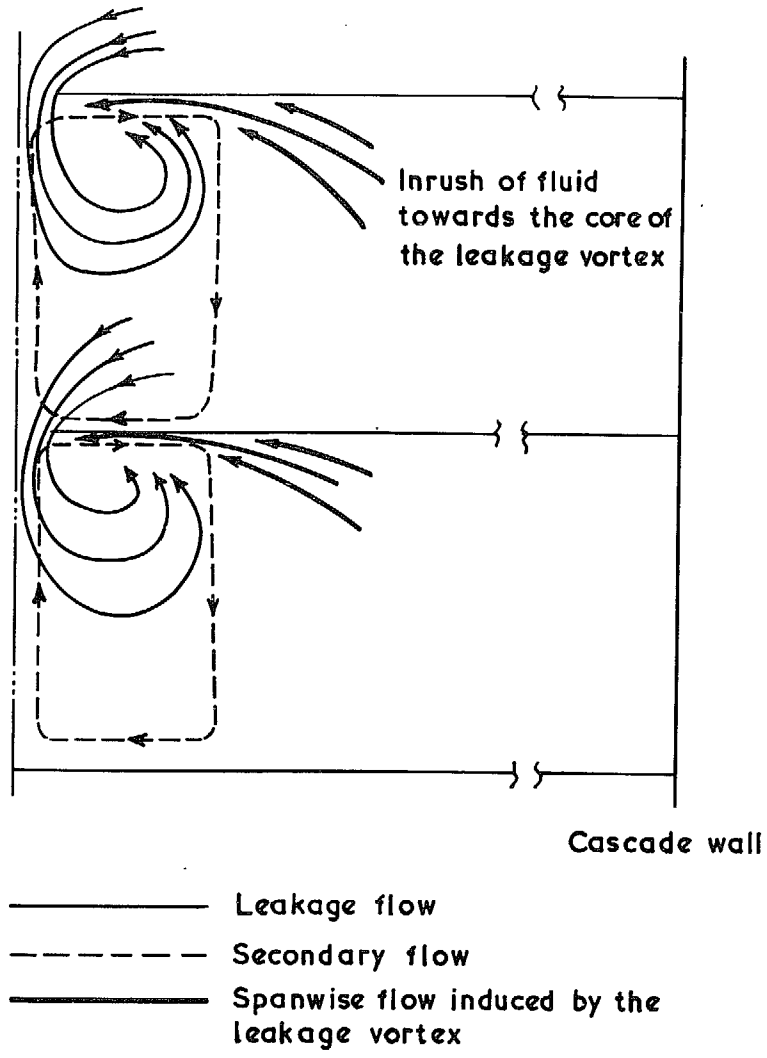

FIG. 20. Nature of leakage and secondary flows in a cascade with non-uniform upstream flow.

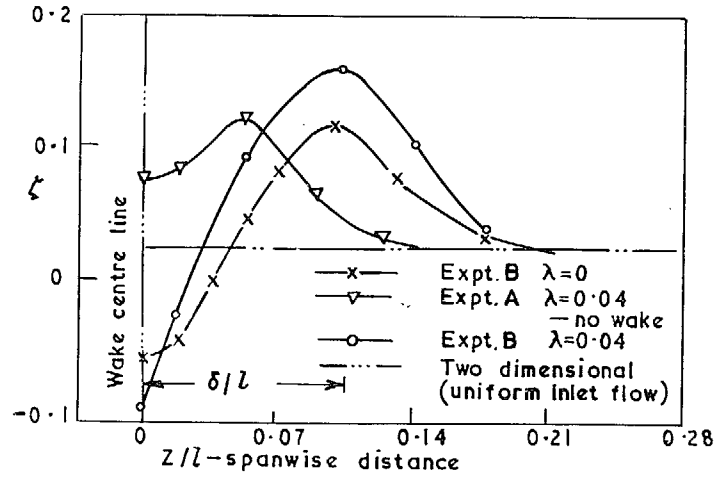

FIG. 21a. Spanwise distribution of loss coefficients for $\lambda = 0$ and 0·04. (Experiments A and B).

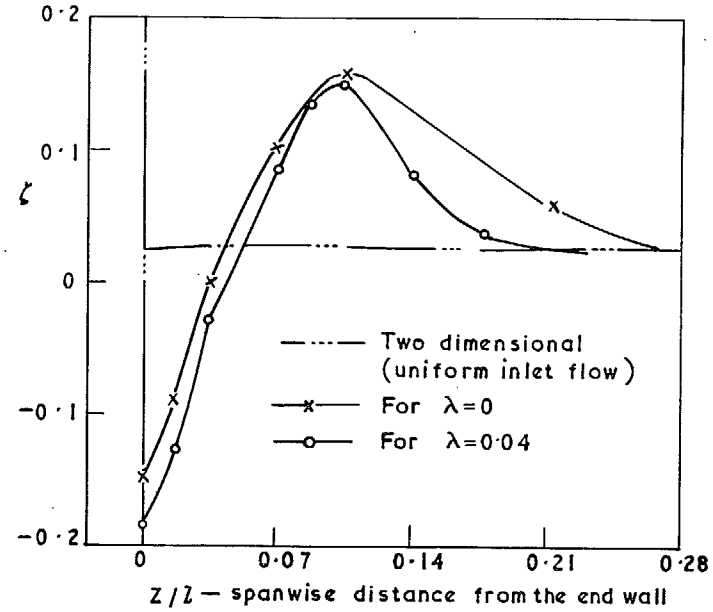

FIG. 21b. Distribution of loss coefficients at outlet in the presence of an end wall. (Experiment C).

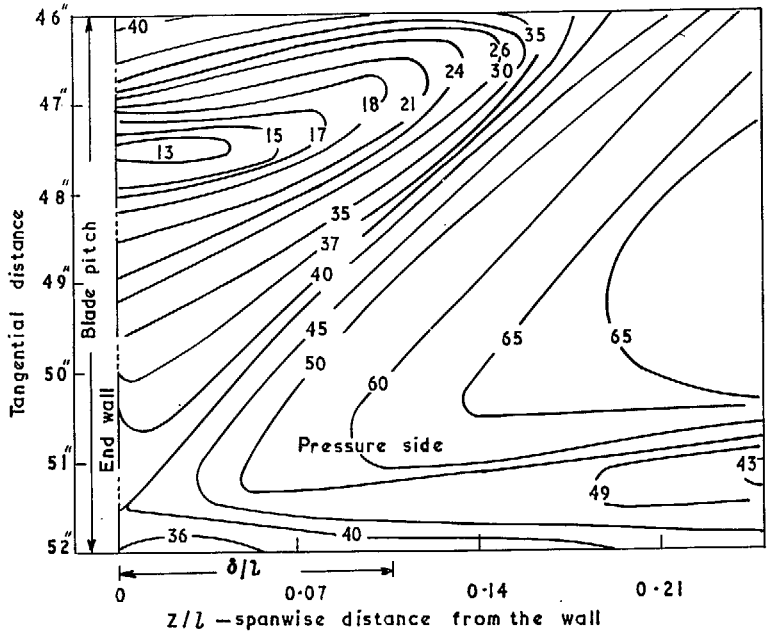

FIG. 22a. Contours of constant dynamic pressure at outlet for $\lambda = 0$. (Experiment C). The numbers on the contours denote the dynamic pressure at outlet as a percentage of reference dynamic pressure at inlet.

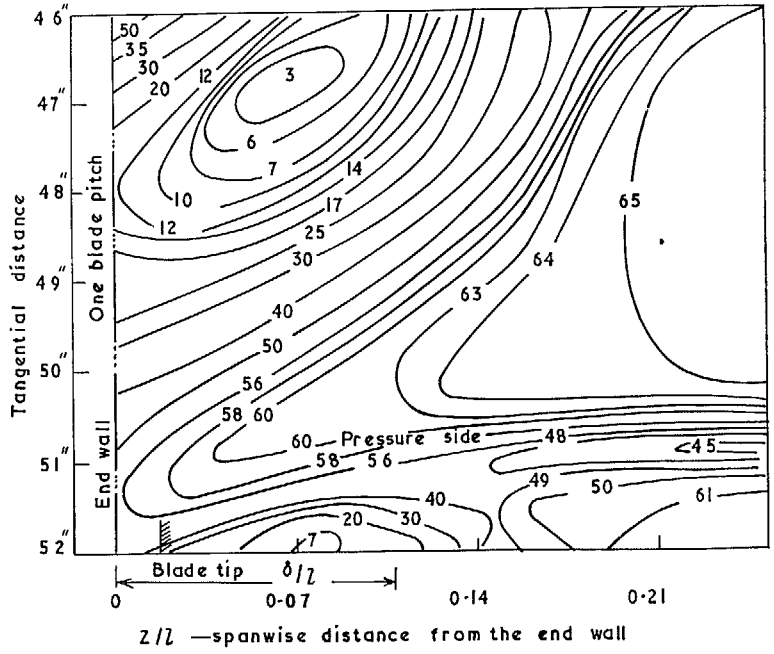

FIG. 22b. Contours of constant dynamic pressure at outlet for $\lambda = 0{\cdot}04$. (Experiment C). The numbers on the contours denote the dynamic pressure at outlet as a percentage of reference dynamic pressure at inlet.

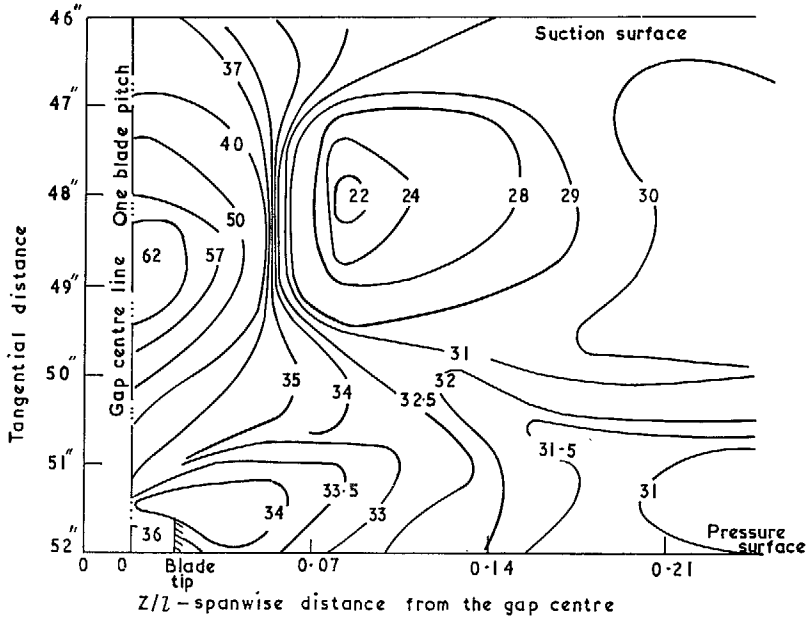

FIG. 23a. Contours of constant outlet angle (α_2) for $\lambda = 0{\cdot}04$ with uniform upstream flow. (Experiment A). Numbers on contours denote outlet angle in degrees.

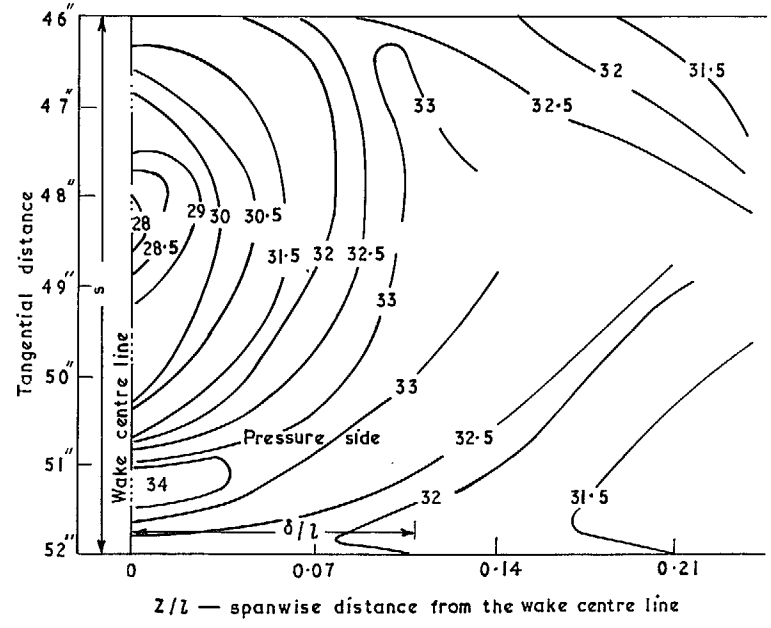

FIG. 23b. Contours of constant outlet angle (α_2) for $\lambda = 0$ with non-uniform upstream flow. (Experiment B). Numbers on the contours denote outlet angle in degrees.

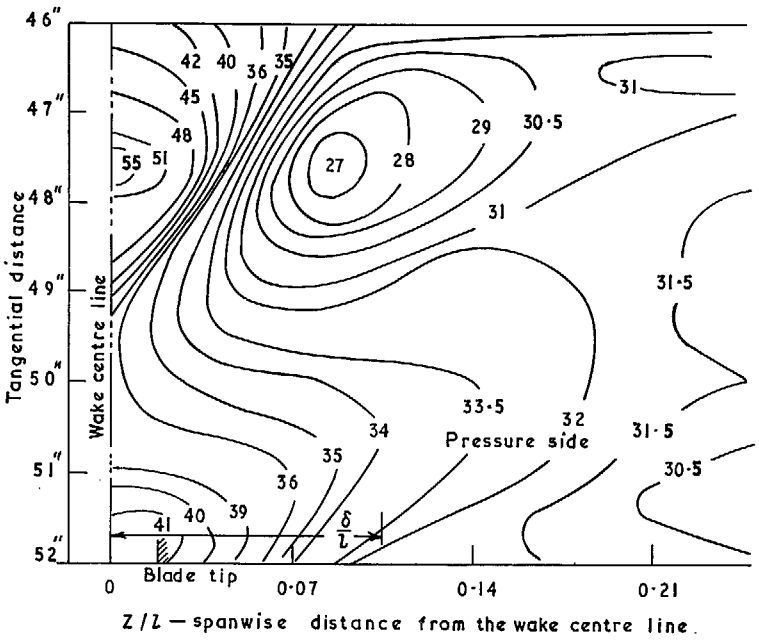

FIG. 23c. Contours of constant outlet angle (α_2) for $\lambda = 0{\cdot}04$ with non-uniform upstream flow. (Experiment B). Numbers on the contours denote outlet angle in degrees.

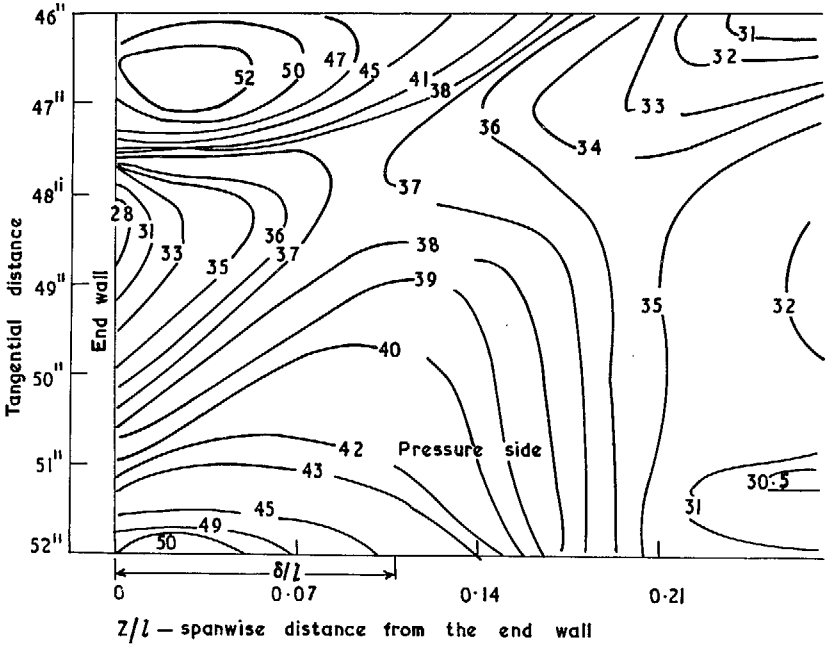

FIG. 24a. Contours of constant outlet angle (α_2) for $\lambda = 0$. (Experiment C). Numbers on the contours denote outlet angle in degrees.

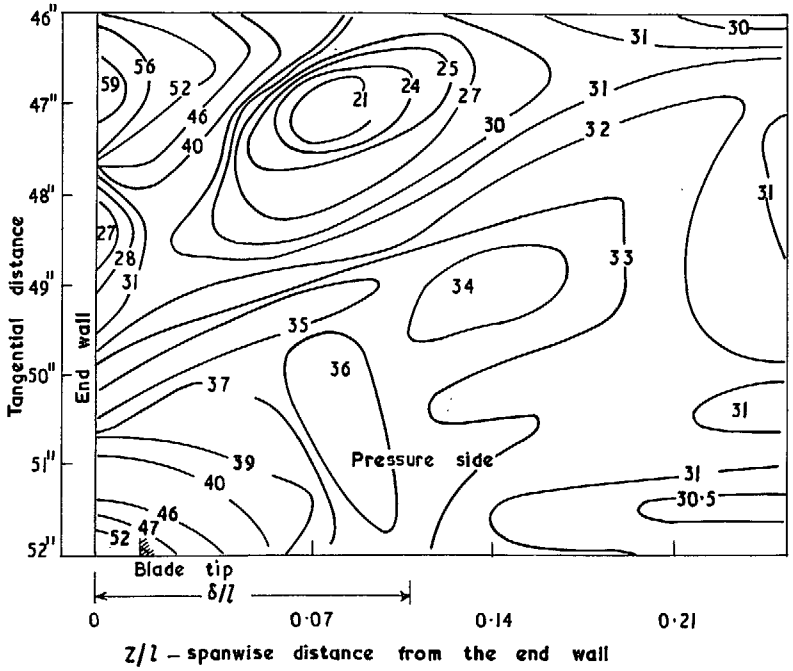

FIG. 24b. Contours of constants outlet angle (α_2) for $\lambda = 0{\cdot}04$. (Experiment C). Numbers on the contours denote outlet angle in degrees.

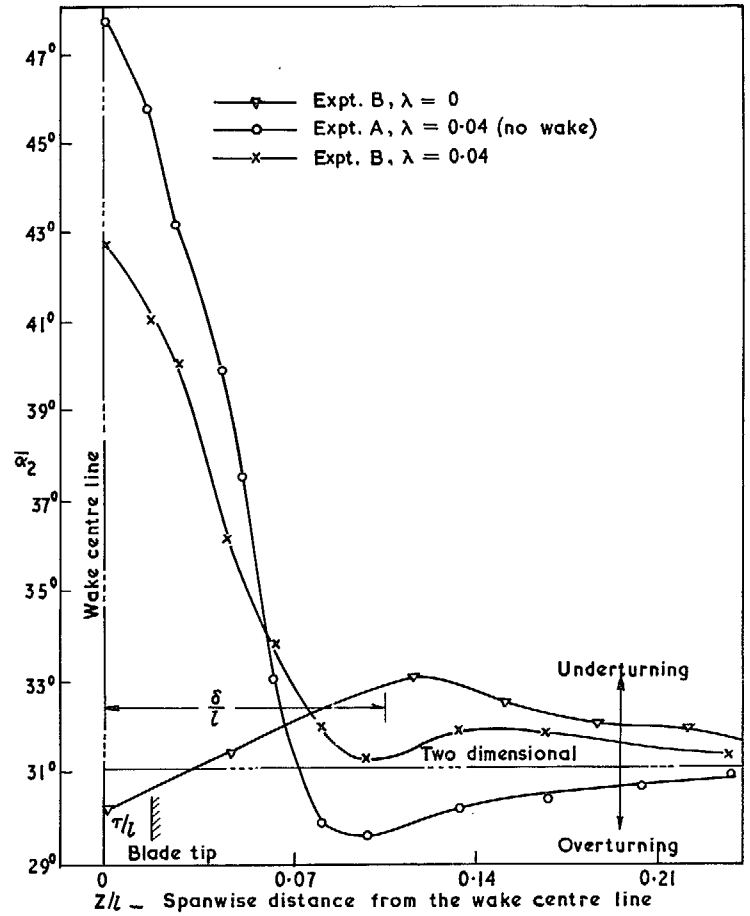

FIG. 25. Comparison of outlet angles (Experiments A and B).

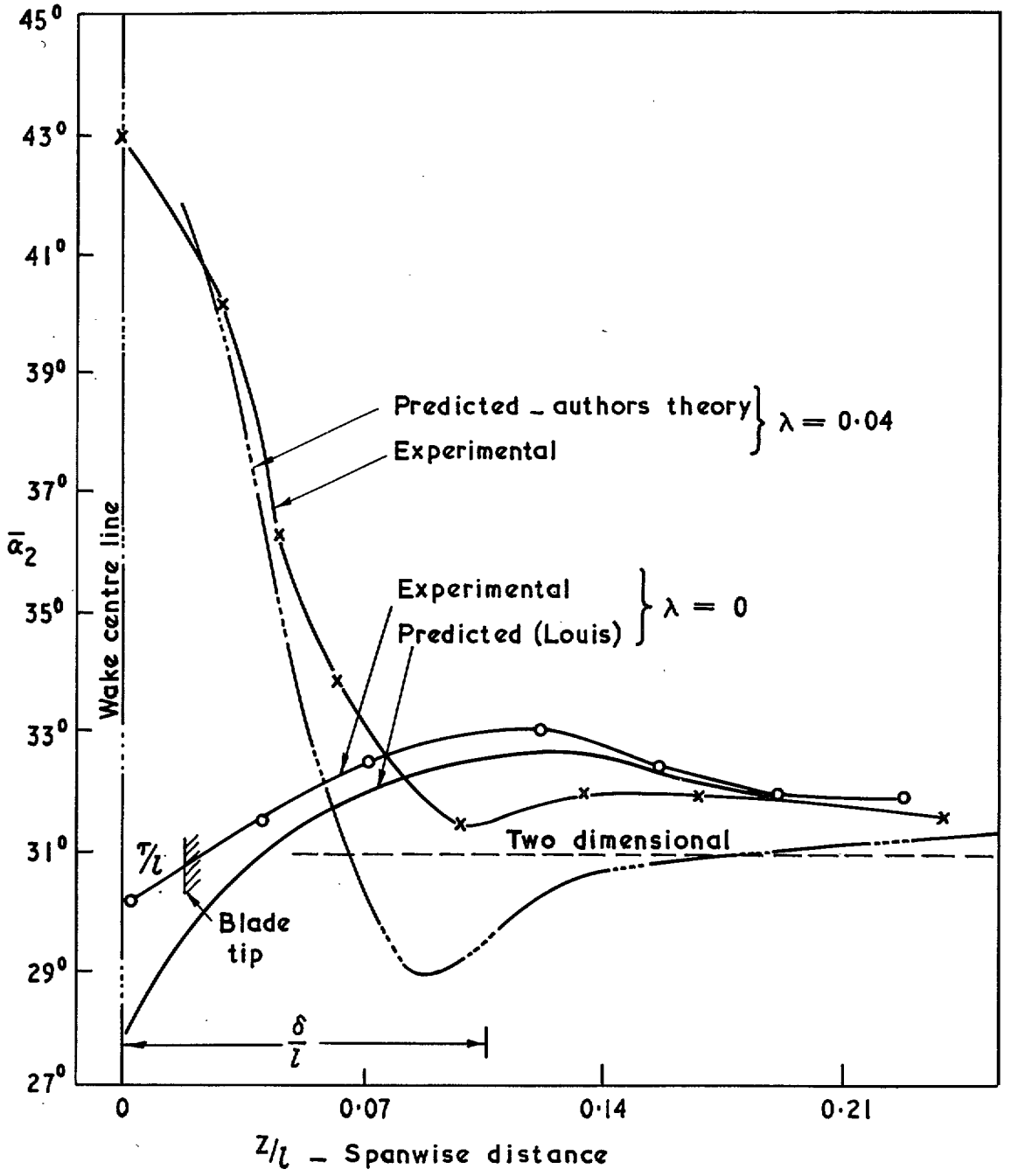

FIG. 26. Predicted and experimental average outlet angles in a cascade with non-uniform inlet flow for $\lambda = 0{\cdot}04$ and $\lambda = 0$ (Experiment B).

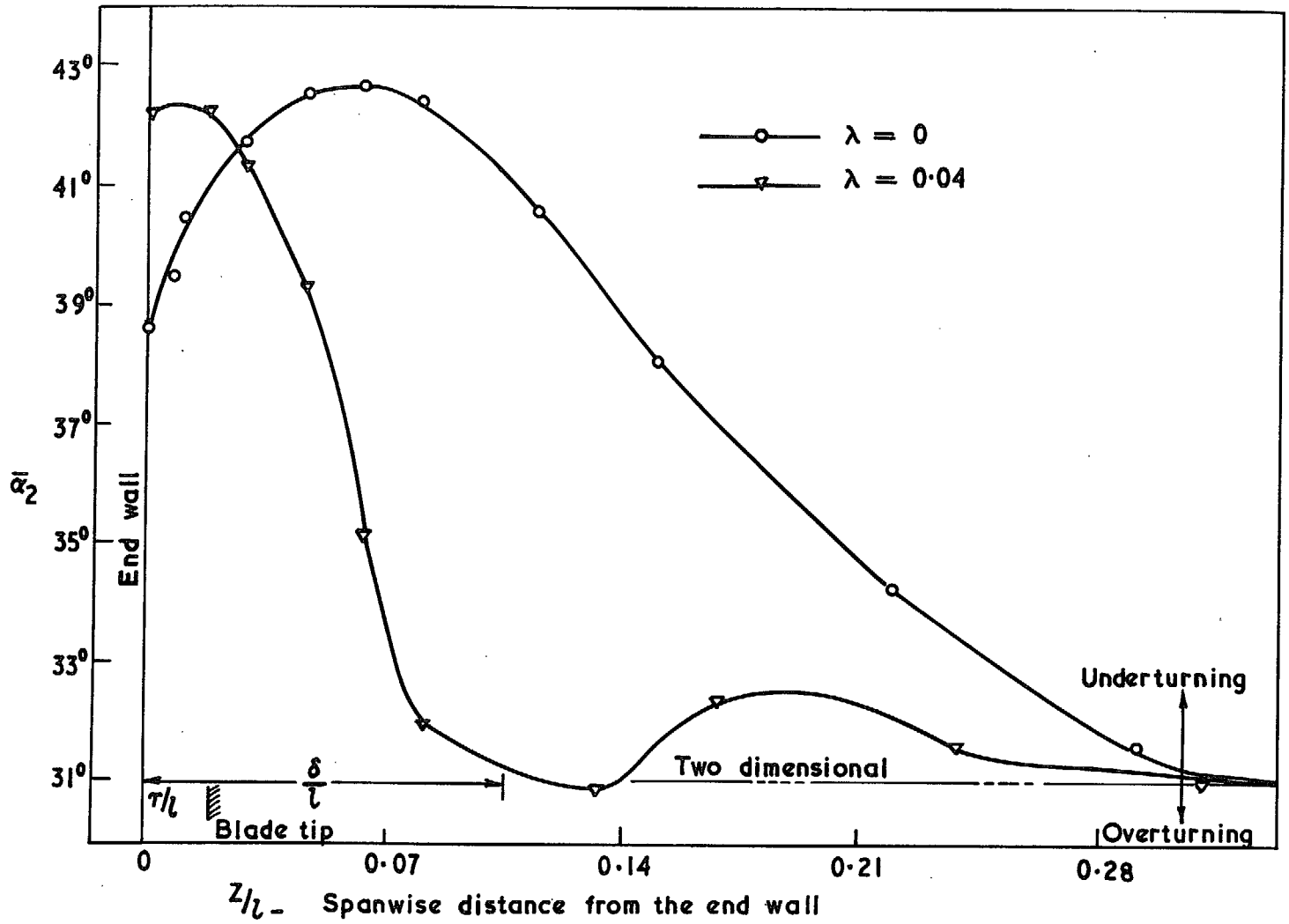

FIG. 27. Average outlet angles for $\lambda = 0$ and $\lambda = 0{\cdot}04$ in the presence of an end wall (Experiment C).

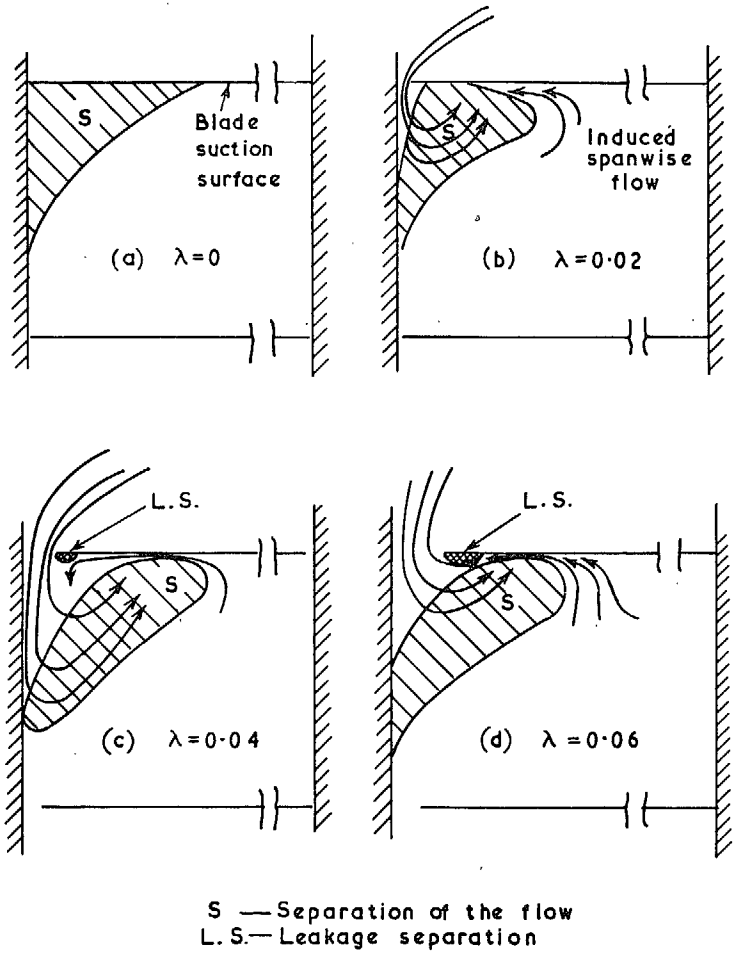

FIG. 29. Diagrammatic representation of separation phenomena on the wall and blade suction surface.

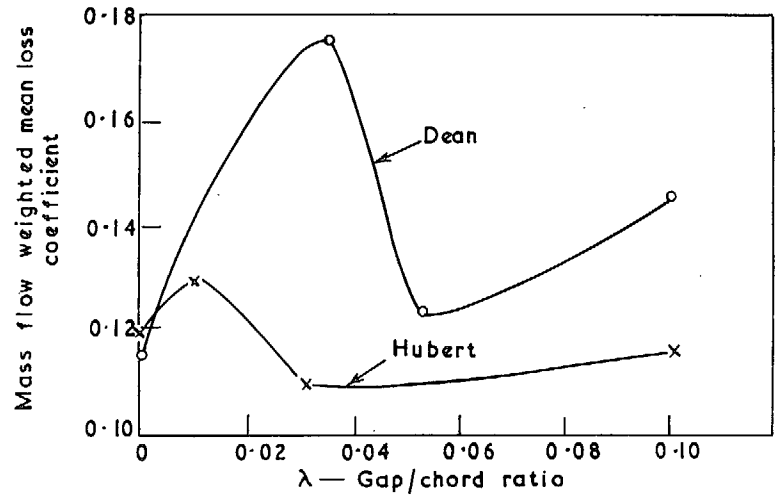

FIG. 30a. Variation of loss coefficient with tip clearance.

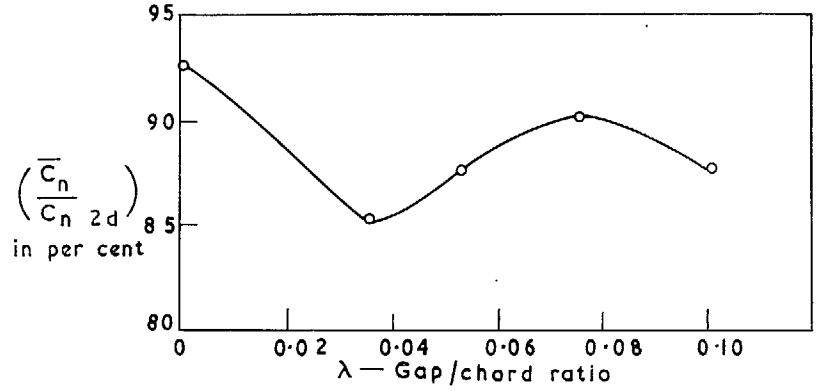

FIG. 30b. Variation uf average normal force with tip clearance (after Dean).

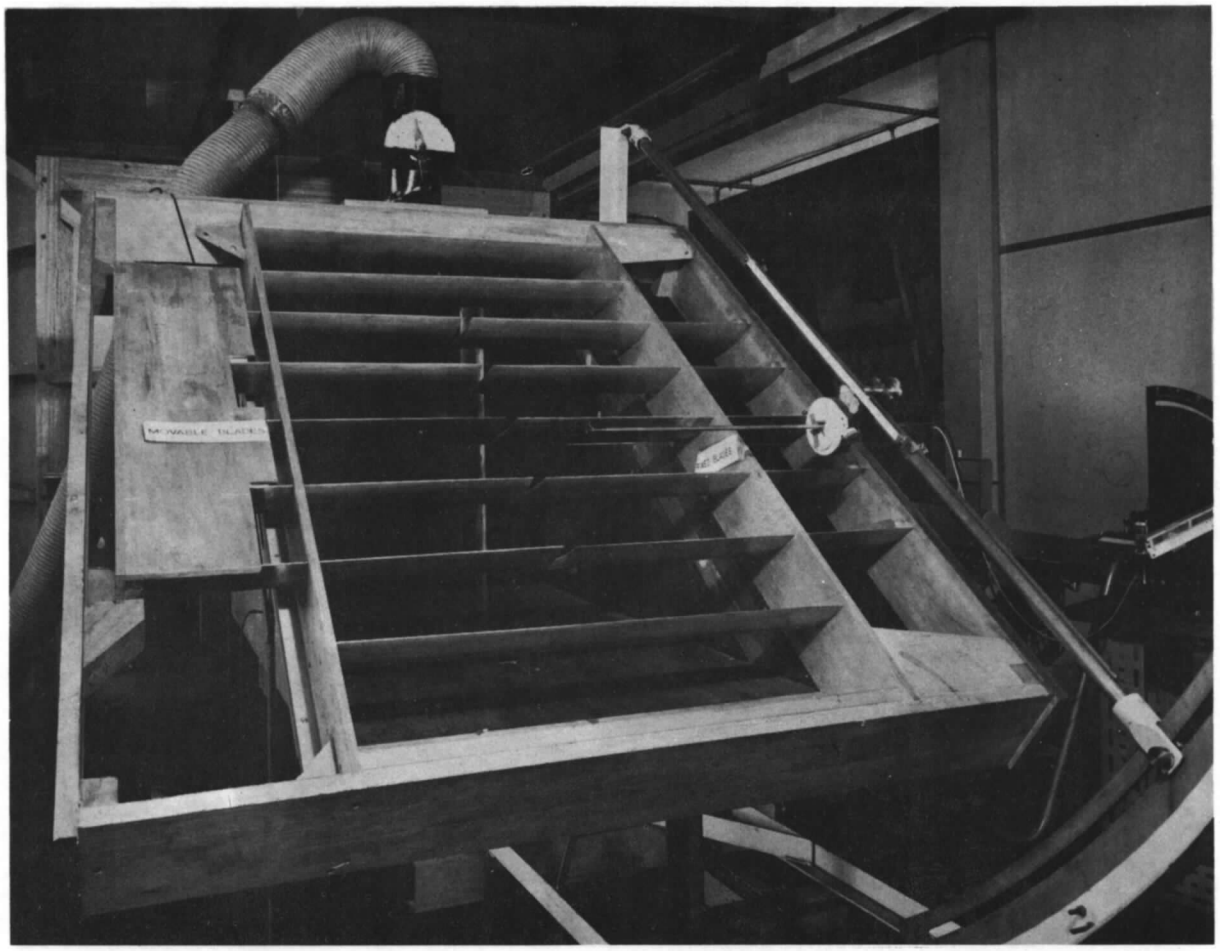

PLATE 1. General arrangement of the cascade and outlet traverse gear.

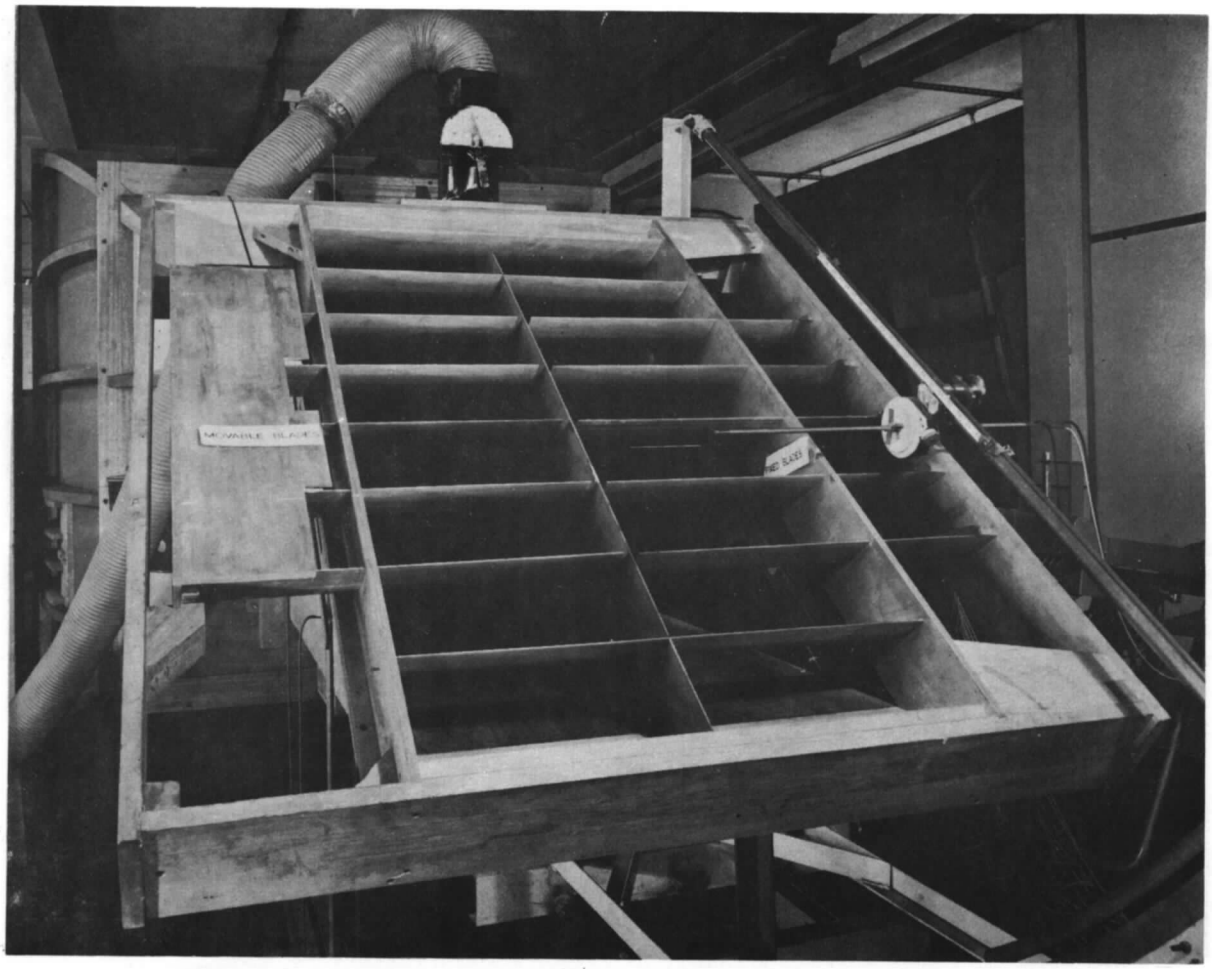

PLATE 2. General arrangement of the cascade with an end wall and tip clearance.

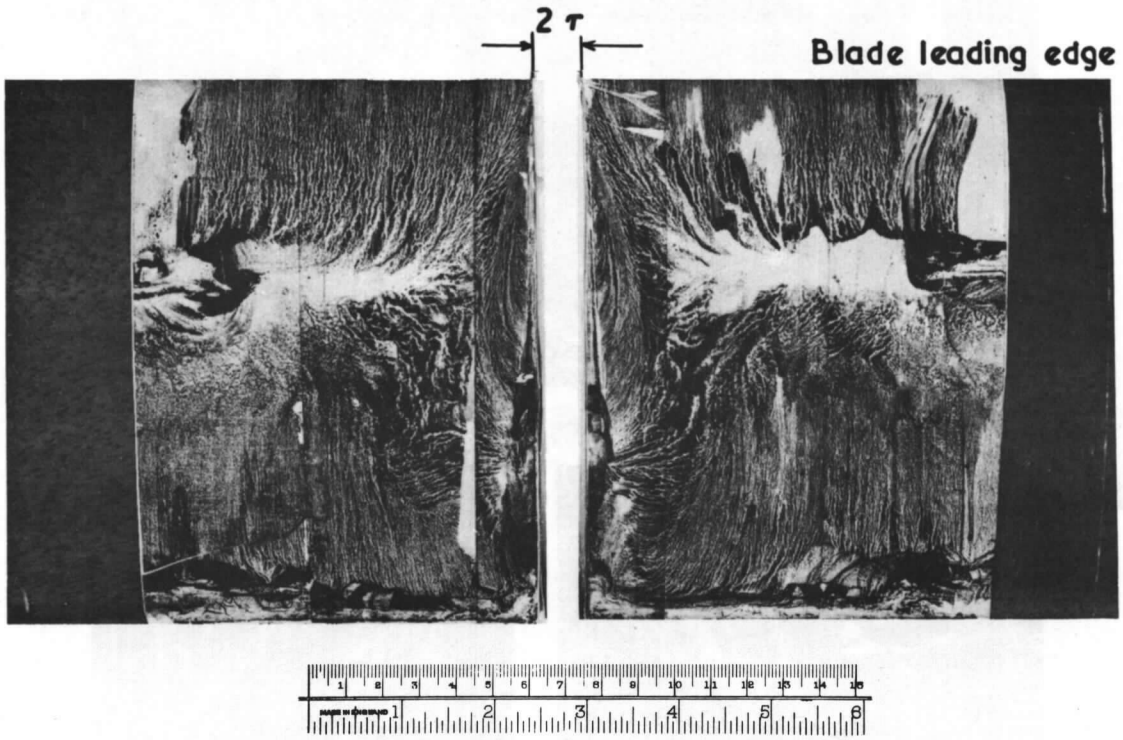

PLATE 3. Streamline traces in carbon black on the blade suction surface for $\lambda = 0{\cdot}04$ (uniform upstream flow – Experiment A).

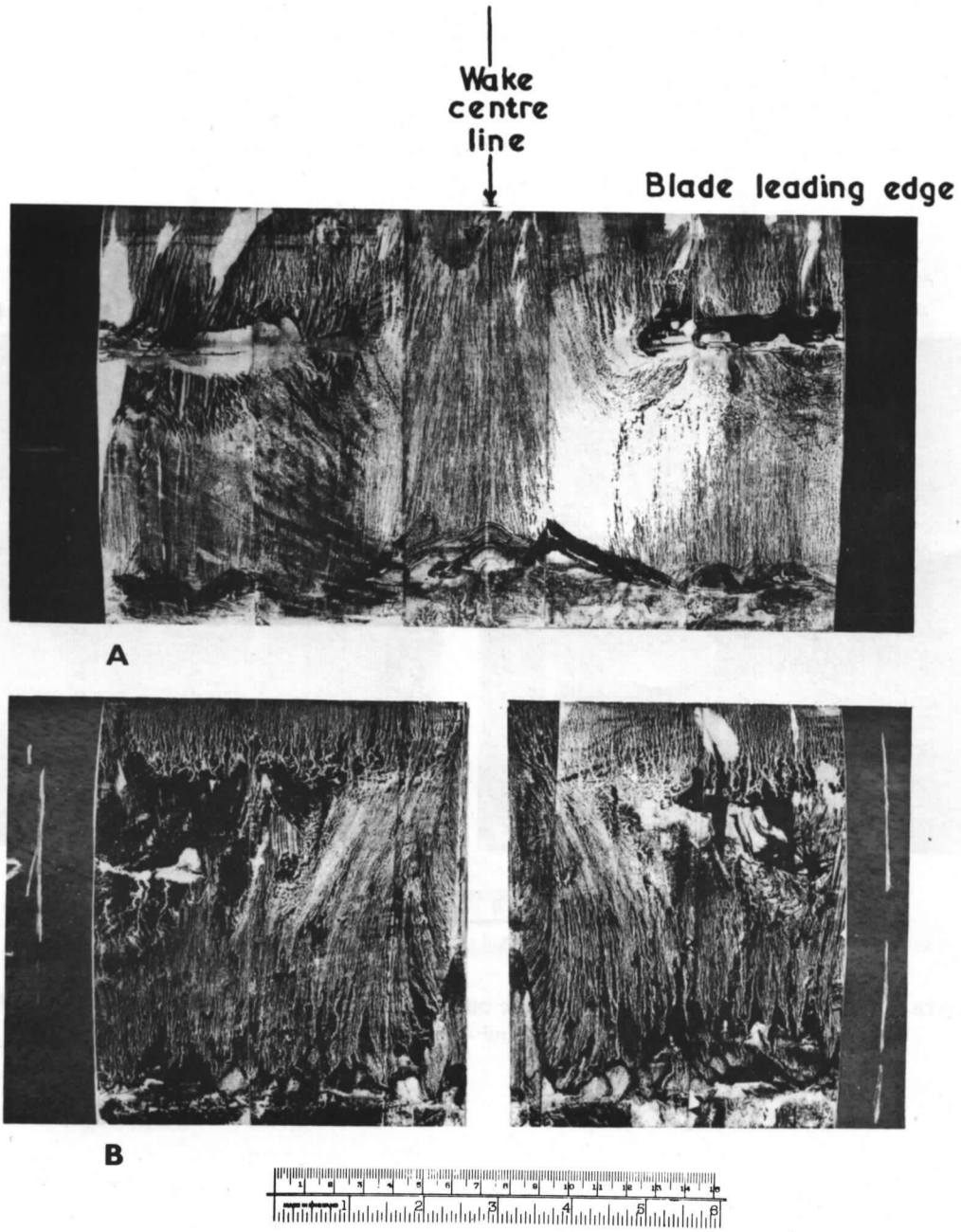

PLATE 4.

Streamline traces in carbon black on the blade suction surface (a) for $\lambda = 0$ and (b) for $\lambda = 0{\cdot}04$ (non-uniform upstream flow – Experiment B).

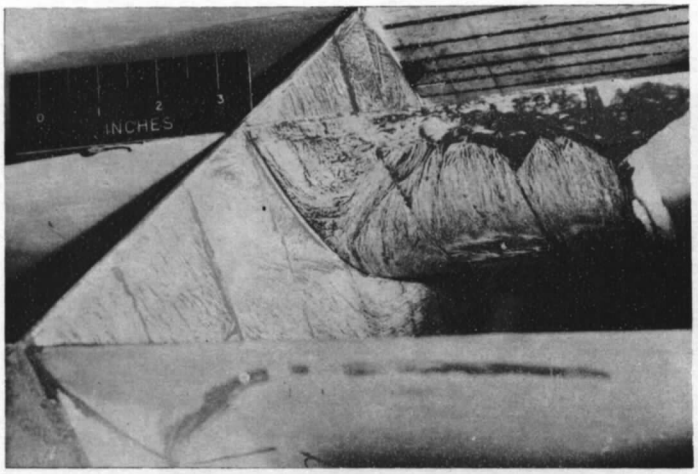

(a)
$\lambda = 0$

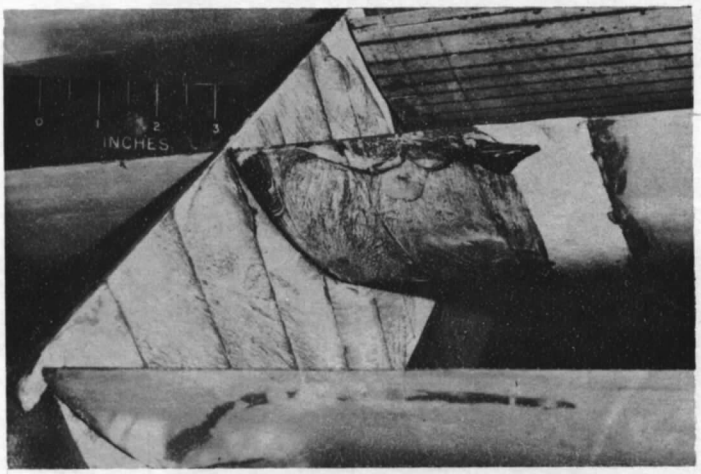

(b)
$\lambda = 0{\cdot}02$

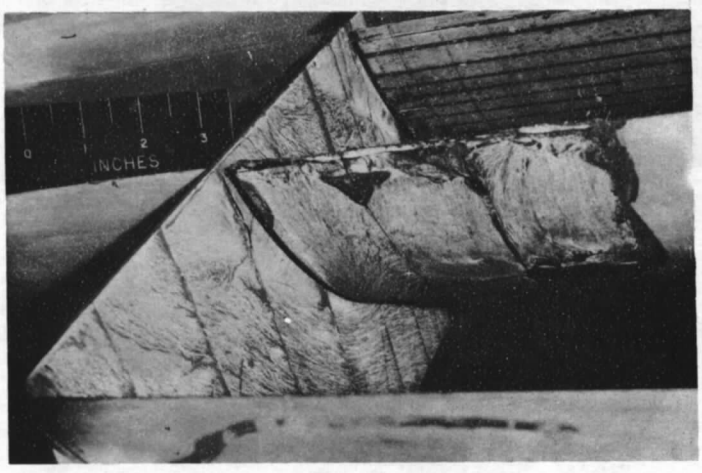

(c)
$\lambda = 0{\cdot}04$

PLATES 5a to c Streamline traces in carbon black on the wall and blade suction surfaces for various gap/chord ratios (Experiment C).

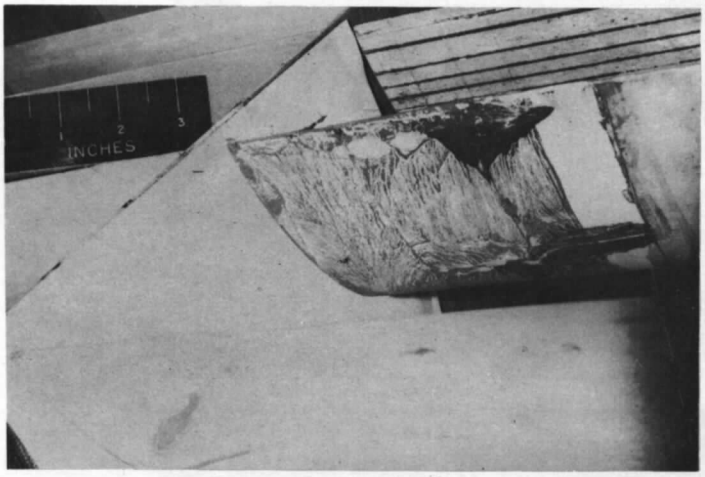

(d)
$\lambda = 0{\cdot}06$

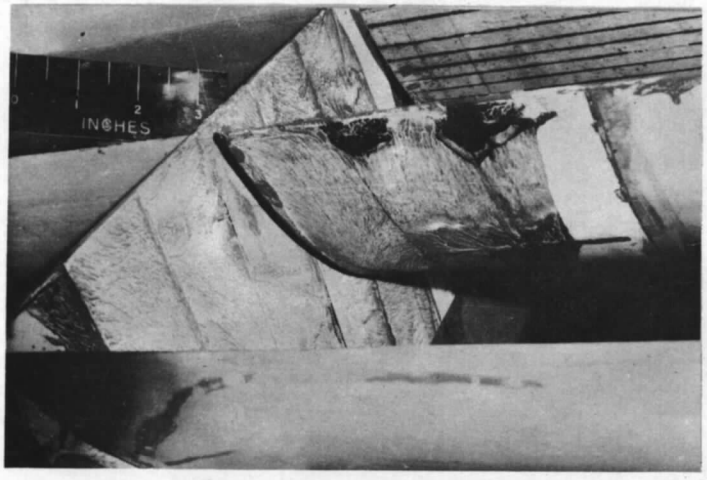

(e)
$\lambda = 0{\cdot}08$

PLATES 5d & e. Streamline traces in carbon black on the wall and blade suction surfaces for various gap/chord ratios (Experiment C).

Printed in Wales for Her Majesty's Stationery Office by Allens Printers (Wales) Limited.

Dd.129527 K5

Published by
HER MAJESTY'S STATIONERY OFFICE

To be purchased from
49 High Holborn, London W.C.1
423 Oxford Street, London W.1
13A Castle Street, Edinburgh 2
109 St. Mary Street, Cardiff
Brazennose Street, Manchester 2
50 Fairfax Street, Bristol 1
35 Smallbrook, Ringway, Birmingham 5
7–11 Linenhall Street, Belfast 2
or through any bookseller

R. & M. No. 3483

S.O. Code No. 23–3483